Rock Mech Rock Eng (2014) 47:2117–2137
DOI 10.1007/s00603-013-0512-6

ORIGINAL PAPER

Three-Dimensional Numerical Investigations of the Failure Mechanism of a Rock Disc with a Central or Eccentric Hole

S. Y. Wang · S. W. Sloan · C. A. Tang

Received: 2 July 2013 / Accepted: 6 November 2013 / Published online: 23 November 2013

Abstract The diametrical compression of a circular disc (Brazilian test) or cylinder with a small eccentric hole is a simple but important test to determine the tensile strength of rocks. This paper studies the failure mechanism of circular disc with an eccentric hole by a 3D numerical model (RFPA3D). A feature of the code RFPA3D is that it can numerically simulate the evolution of cracks in three-dimensional space, as well as the heterogeneity of the rock mass. First, numerically simulated Brazilian tests are compared with experimental results. Special attention is given to the effect of the thickness to radius ratio on the failure modes and the peak stress of specimens. The effects of the compressive strength to tensile strength ratio (C/T), the loading arc angle (2α), and the homogeneity index (m) are also studied in the numerical simulations. Secondly, the failure process of a rock disc with a central hole is studied. The effects of the ratio of the internal hole radius (r) to the radius of the rock disc (R) on the failure mode and the peak stress are investigated. Thirdly, the influence of the vertical and horizontal eccentricity of an internal hole on the initiation and propagation of cracks inside a specimen are simulated. The effect of the radius of the eccentric hole and the homogeneity index (m) are also investigated.

S. Y. Wang (✉) · S. W. Sloan
ARC Centre of Excellence for Geotechnical Science and Engineering, Civil, Surveying and Environmental Engineering, The University of Newcastle, Callaghan, NSW 2308, Australia
e-mail: Shanyong.Wang@newcastle.edu.au

S. W. Sloan
e-mail: Scott.Sloan@newcastle.edu.au

C. A. Tang
School of Civil and Hydraulic Engineering, Dalian University of Technology, Dalian 116024, People's Republic of China
e-mail: catang@mechsoft.cn

Keywords Rock · Brazilian test · Eccentricity · 3D numerical simulation · Crack initiation and propagation

1 Introduction

Since the tensile strength of rock is much lower than its compressive strength, many failures in rock engineering are caused by the initiation, propagation and coalescence of tensile fractures inside a rock mass. The Brazilian test is widely adopted to determine the tensile strength of rock as an alternative to the direct uniaxial tensile test due to its simplicity in preparing samples (Berenbaum and Brodie, 1959; Bieniawski and Hawkes 1978). According to ISRM (1978), the indirect tensile strength of a disc sample (Fig. 1) is given by

$$\sigma_t = \frac{2P}{\pi dt} \tag{1}$$

where d is the diameter, t is the thickness, and P is the applied diametrical load.

If the rock is assumed to be elastic and isotropic, the elastic solution of Jaeger and Cook (1979) can be used to determine the stress field inside the disc. The three-dimensional correction to this two-dimensional solution has been given by Wijk (1978). However, since rock is a heterogeneous material which has non-linear stress/strain characteristics, the actual stress field that causes tensile failure in a Brazilian test is not easy to determine by analytical methods. Thus, there may be serious discrepancies between the theoretical predictions and actual values for the tensile strength (Mellor and Hawkes 1971).

According to the Griffith criterion (Griffith 1920), the uniaxial strength can be determined accurately from the

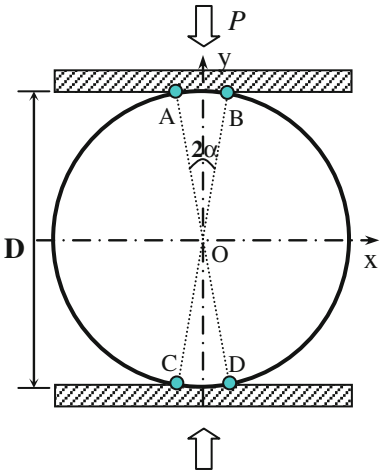

Fig. 1 Geometrical parameters and loading conditions for standard Brazilian disc

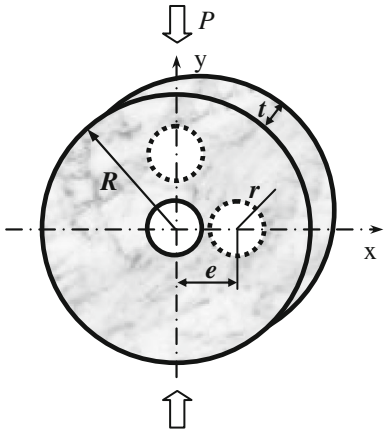

Fig. 2 Diametrically loaded disc with a hole: geometrical configuration

Brazilian test when the tensile failure occurs at the centre of the disc. Fairhurst (1964), however, reported that failure may occur away from the centre of the test disc when small loading arc angles are considered or when the compressive strength is not dramatically greater than the tensile strength. Fairhurst's empirical generalization of the fracture criterion for the Brazilian tensile test overcomes the criticism of the Griffith criterion that the predicted ratio of the uniaxial compressive strength to the uniaxial tensile strength (8:1) is usually lower than that observed. Erarslan et al. (2012) conducted both experimental and numerical tests to investigate the influence of loading arc angles in Brazilian tests. Their results indicate that the ultimate failure load increases with increasing loading arc angles, with angles of 20° or more resulting in diametric splitting fractures at the disc centre. These observations support the results of Fairhurst (1964).

Mellor and Hawkes (1971) claim that the Brazilian test is capable of giving a good measure of the uniaxial tensile strength for Griffth-type materials when it is performed carefully, i.e. special attention should be paid to the control of contact stresses and accurate load measurement, as well as other factors such as the specimen dimensions, load rates, and contact zones. Otherwise, the results obtained using this technique are questionable because wedge-shaped fractures frequently form beneath the loading platens rather than tensile failure occurring along the loaded diameter (Hobbs 1965). To overcome this shortcoming, ring specimens have also been developed where a disc with a central hole is subjected to diametric compression (Ripperger and Davids 1947; Hobbs 1964; Hudson 1969). In ring tests, failure initiates in a uniaxial stress field, but steep stress gradients are required to propagate the resulting crack. For ring tests, the calculated tensile strength for Griffith-type materials is much larger than the uniaxial tensile strength when the hole size is very small. As the hole size is increased, the calculated strength tends asymptotically towards the modulus of rupture (flexural strength) (Mellor and Hawkes 1971). According to Hobbs (1965), the maximum tensile stress σ_t is given by

$$\sigma_t = \frac{P}{\pi R t}\left(6 + 38\left(\frac{r}{R}\right)^2\right) \tag{2}$$

while the maximum compressive stress σ_c is

$$\sigma_c = \frac{P}{\pi R t}\left(10 + 10\left(\frac{r}{R}\right)^2\right) \tag{3}$$

where r is the internal radius, R is the external radius of the disc, and t is the thickness of the disc (see Fig. 2). The eccentricity of the internal hole influences the inferred estimate of the tensile strength. (Hobbs 1965). When the centre of the hole lies on the line of the vertical diametric load, as shown in Fig. 2, the maximum tensile stress around the hole is given by

$$\sigma_{tv} = \frac{P}{\pi R t}\left(2 + \frac{2R}{R-e} + \frac{2R}{R+e}\right) \tag{4}$$

where the eccentricity e is the distance between the centre of the hole and the centre of disc. In contrast, when the centre of the hole lies on the diameter perpendicular to the line of loading, the maximum tensile stress is given by

$$\sigma_{th} = \frac{P}{\pi R t}\frac{2(3R^2 - e^2)(R^2 - e^2)}{(R^2 + e^2)^2} \tag{5}$$

Based on this analysis, discs tested with a concentric hole probably give rise to an error in the tensile strength of around 5 % (Hobbs 1965).

Van De Steen et al. (2005) carried out both experimental and numerical tests to study the fracture pattern for a loaded disc with an eccentric hole. Their results indicate that changing either the diameter of the hole or its eccentricity

affects the tensile stress and the stress gradient at the hole surface. Whether the final failure intersects the hole or occurs by diametral splitting depends on the radius and eccentricity of the hole.

The fracture process of rock at the laboratory (macro-scale) scale can be simulated numerically using the Boundary Element Method (BEM), the Finite Element Method (FEM) or the Discrete Element Method (DEM). Chen et al. (1998) developed a new BEM code to simulate the failure process of an anisotropic rock disc with a pre-existing crack at the centre. The maximum tensile stress failure criterion was adopted to predict the crack initiation direction and propagation path. Lavrov et al. (2002) used the DIGS simulation code to study the Kaiser effect in cyclic Brazilian tests with disc rotation. The micro-fractures and associated acoustic emission evolutions were reproduced. Cai and Kaiser (2004) applied a coupled FEM/DEM approach to simulate crack initiation and propagation in Brazilian tests, considering both isotropic and anisotropic behaviour. Zhu and Tang (2006) used the RFPA (Rock Failure Process Analysis) code to simulate the deformation and failure of a Brazilian disc subjected to static and dynamic loading, taking into account the heterogeneity of the rock mass. Yu et al. (2006) adopted the 3D-FEM to calculate the tensile stresses in a Brazilian disc with a thickness to diameter ratio (t/D) varying from 0.2 to 1. For specimens with a high ratio ($0.5 < t/D < 1$), they found that the tensile stresses at the two end surfaces are relatively high and it is easy to exceed the tensile strength leading to breakage of the specimen (Yu et al. 2006). Furthermore, Yu et al. (2009) conducted a modified Brazilian test to solve the problems of stress concentration and higher t/D ratios existing in the traditional Brazil test. Lanaro et al. (2009) used the BEM to numerically simulate the influence of cracks initiation on the stress distribution within a Brazilian disc. Erarslan and Williams (2012a) employed the numerical tool RFANC2D to investigate the effect of a pre-existing crack on the stress distribution within Brazilian test specimen, where the material was assumed to be homogenous and isotropic. Bahrani et al. (2012) used the code PFC2D (a two-dimensional particle flow code) with a grain-based model to predict the failure process of a Brazilian test on Brisbane tuff. The stress–strain curve, as well as inter-grain tensile cracking and shear cracking, were simulated. Finally, Van de Steen et al. (2005) used the boundary element code DIGS to study the fracturing behaviour of a diametrically loaded disc with an eccentric hole. Jiao et al. (2012) developed a new contact constitutive model and incorporated it into the discontinuous deformation analysis (DDA) code to investigate the fractures' evolution in a Brazilian disc with an eccentric hole. Sun et al. (2013) used particle manifold method (PMM), which is an extension and improvement of the numerical manifold method (NMM) to numerically simulate the failure mode of Brazilian disc. However, most of these models were limited to two-dimensional situations. Moreover, the heterogeneity of rock was not considered, and the evolution of cracks in the specimen was not well captured.

In this study, the code RFPA3D, which is an extension of RFPA2D, is applied to investigate the 3D fracturing processes of Brazilian specimens with/without a central/eccentric hole. First, the numerical predictions for

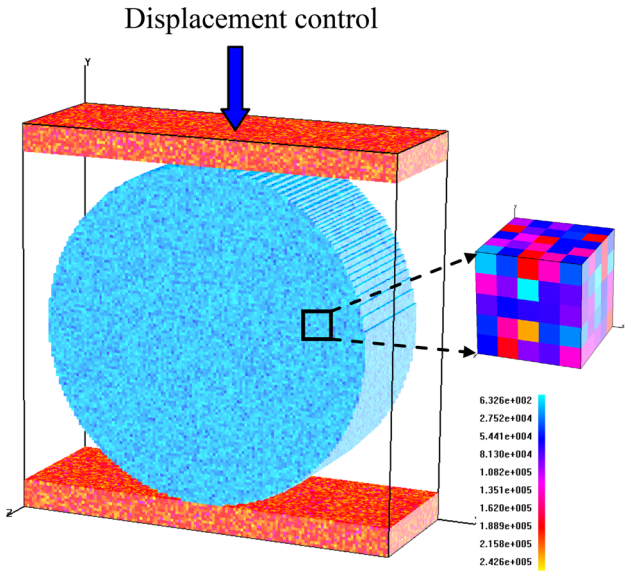

Fig. 3 Numerical model for standard Brazilian disc

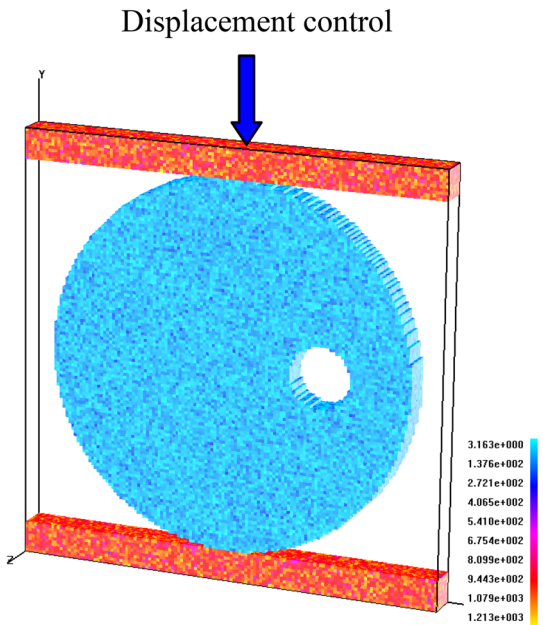

Fig. 4 Numerical model for diametrically loaded disc with a hole

Brazilian tests are compared with previously published experimental results. Special attention is given to the effect of the thickness to radius ratio on the failure mode and peak stress of the specimens. The effects of the ratio of the compressive strength to the tensile strength, as well as the loading arc angle, are considered, together with the influence of the homogeneity index (m). Secondly, the failure process of a rock disc with a central hole is simulated numerically, and the effect of the ratio r/R on the failure mode and peak stress is evaluated. Thirdly, the influence of the vertical and horizontal eccentricity of an internal hole on the initiation and propagation of cracks inside a specimen are simulated. The effect of the radius of the eccentric hole and the homogeneity index (m) are also investigated

2 Brief Description of RFPA3D

RFPA3D is based on the two-dimensional code RFPA2D (Tang 1997). Similar, to the latter, RFPA3D assumes that

Table 1 Weibull distribution parameters used for RFPA^{3D} to simulate Brisbane tuff (Erarslan and Williams 2012b)

Materials	Homogeneity index m	Mean of Young's modulus (GPa)	Poisson's ratio	Mean of uniaxial compressive strength (MPa)	Mean of uniaxial tensile strength
Rock	2	25	0.26	190	15
Cardboard	Homogeneous	10	0.3	500	1

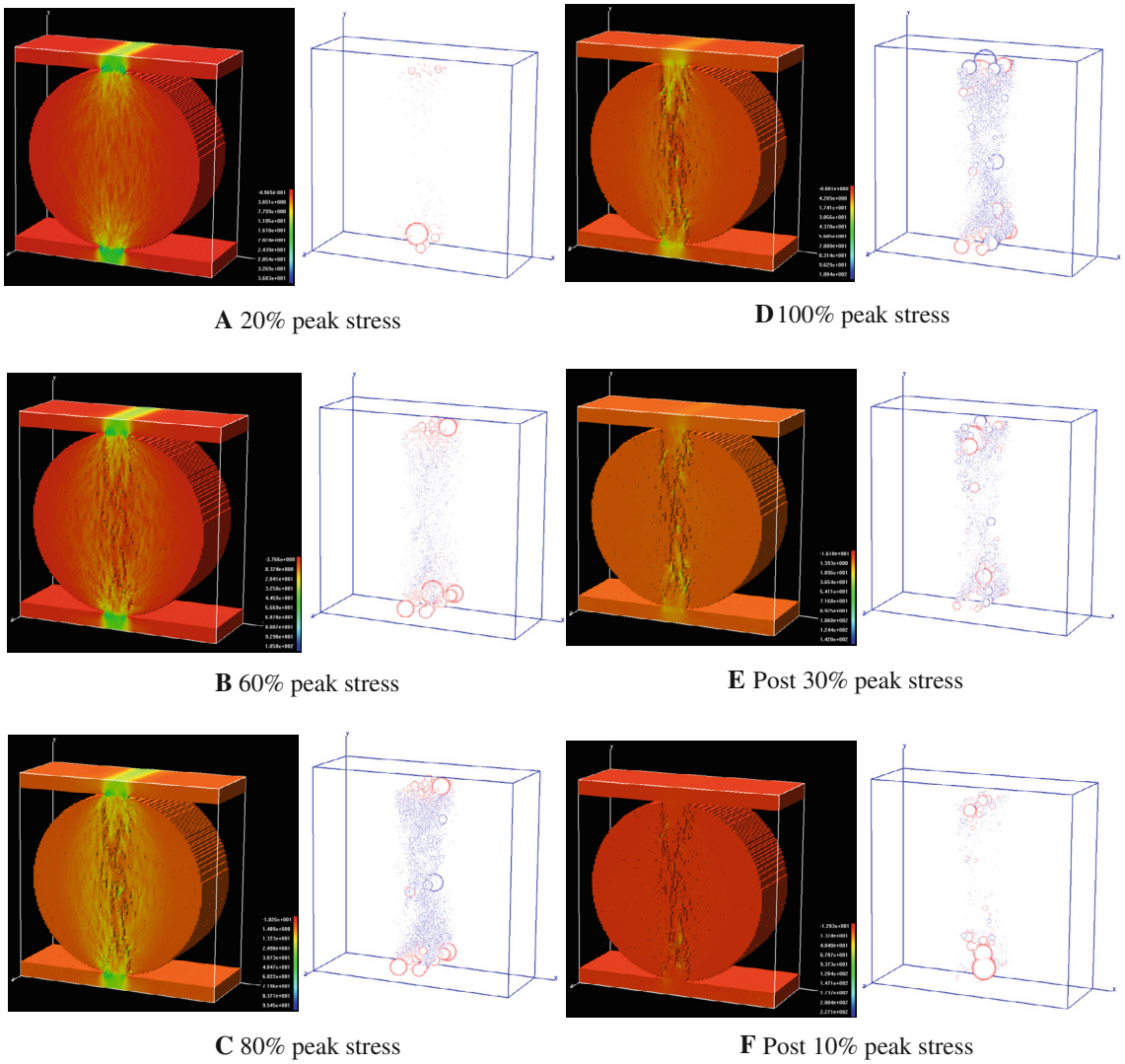

Fig. 5 3D numerically simulated failure process of Brazilian discs: maximum principal stress distribution and acoustic emission distribution

the domain consists of elements with the same shape and size and that there is no geometric priority in any orientation (Tang 1997; Wang et al. 2006). The elemental mechanical parameters (i.e. uniaxial compressive strength, the elastic modulus and Poisson's ratio) are described by a certain statistical distribution such as the Weibull distribution function (Weibull 1951) as follows:

$$W(x) = \frac{m}{x_0}\left(\frac{x}{x_0}\right)^{m-1} \exp\left[-\left(\frac{x}{x_0}\right)^{m}\right] \quad (6)$$

where x is a given mechanical property (such as the strength or elastic modulus), x_0 is a scaling parameter, and m is defined as the homogeneity index that determine the shape of the distribution function. As the homogeneity index increases, the material becomes more homogeneous (Tang 1997).

A linear elastic damage law is adopted to model the mechanical behaviour of the meso-scale elements. For each element, the material is assumed to be linear elastic, isotropic and damage-free before loading. After the initiation of damage, the elastic modulus of an element is supposed to degrade monotonically as the damage evolves according to the relation (Tang et al. 2007; Wang et al. 2011, 2012a):

$$E = (1 - D)E_0 \quad (7)$$

where D represents the damage variable, and E and E_0 are the elastic modulus of the damaged and the undamaged material, respectively.

The constitutive relationship of a mesoscopic element under uniaxial tension is expressed as (Zhu and Tang 2006; Wang et al. 2012b):

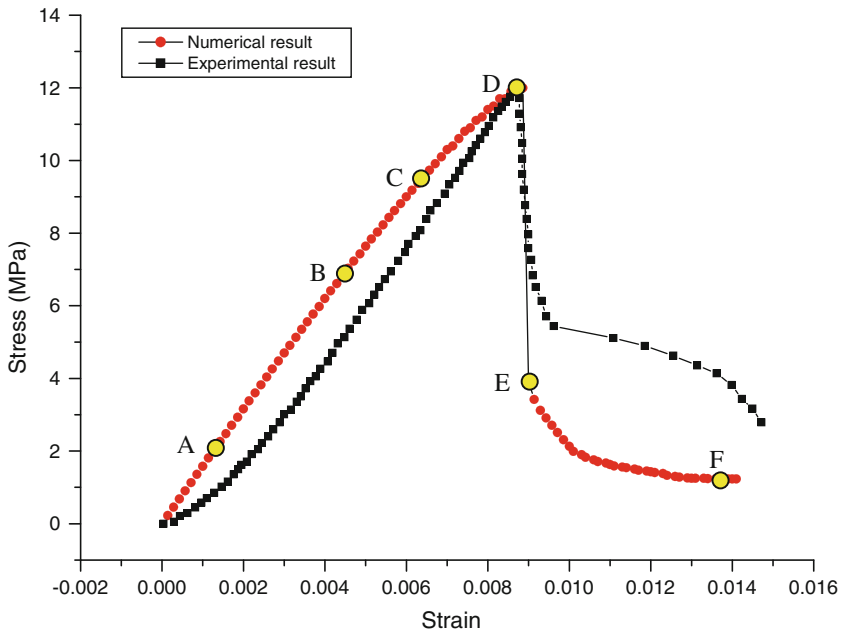

Fig. 6 Comparison of numerically simulated stress–strain curves with experimental results for standard Brazilian tests (after Erarslan and Williams 2012b)

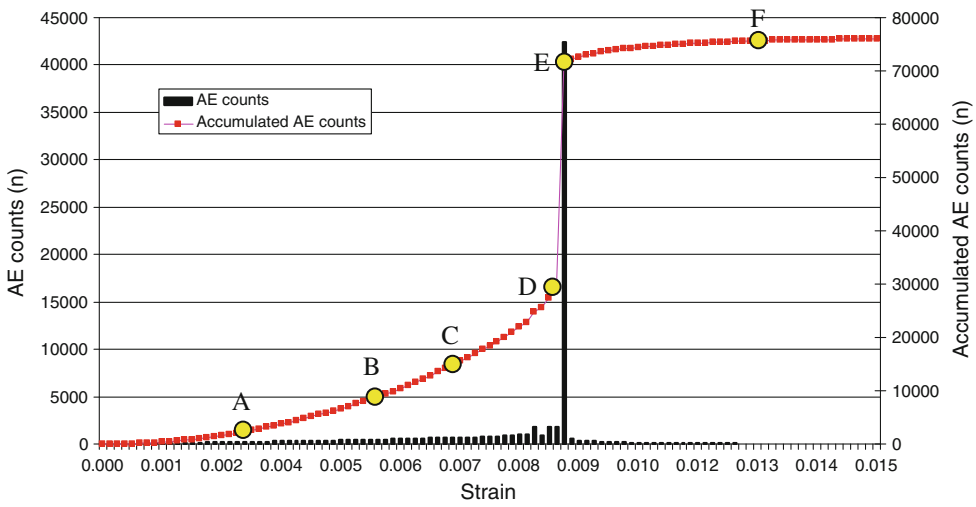

Fig. 7 Numerically simulated acoustic emission counts and accumulated acoustic emission counts during the failure process of standard Brazilian tests

Fig. 8 Observed failure modes in the Brazilian test on Brisbane tuff (after Erarslan and Williams 2012b)

$$D = \begin{cases} 0 & \varepsilon < \varepsilon_{t0} \\ 1 - \frac{f_{tr}}{E_0 \varepsilon} & \varepsilon_{t0} \le \varepsilon \le \varepsilon_{tu} \\ 1 & \varepsilon > \varepsilon_{tu} \end{cases} \tag{8}$$

where f_{tr} is the residual tensile strength, which is given as $f_{tr} = \lambda f_{t0} = \lambda E_0 \varepsilon_{t0}$; f_{t0} and λ are the uniaxial tensile strength and residual strength coefficients, respectively; ε_{t0} is the strain at the elastic limit, which is termed the threshold strain; and ε_{tu} is the ultimate tensile strain at which the element would be completely damaged. The ultimate tensile strain is defined as $\varepsilon_{tu} = \eta \varepsilon_{t0}$, where η is the ultimate strain coefficient. Equation (8) can also be expressed as (Zhu and Tang 2006; Wang et al. 2011):

$$D = \begin{cases} 0 & \varepsilon < \varepsilon_{t0} \\ 1 - \frac{\lambda \varepsilon_{t0}}{\varepsilon} & \varepsilon_{t0} \le \varepsilon \le \varepsilon_{tu} \\ 1 & \varepsilon > \varepsilon_{tu} \end{cases} \tag{9}$$

In addition, it is assumed that the damage to mesoscopic elements under multiaxial stress conditions is also isotropic and elastic (Tang 1997). Under multiaxial stress states, the element can still be damaged in the tensile mode when the equivalent major tensile strain $\bar{\varepsilon}$ exceeds the threshold strain ε_{t0}. The equivalent principal strain $\bar{\varepsilon}$ is defined as (Wang et al. 2011):

$$\bar{\varepsilon} = \sqrt{\langle \varepsilon_1 \rangle^2 + \langle \varepsilon_2 \rangle^2 + \langle \varepsilon_3 \rangle^2} \tag{10}$$

where ε_1, ε_2 and ε_3 are the principal strains and $\langle\rangle$ denotes Macaulay's function:

$$\langle x \rangle = \begin{cases} x & x \ge 0 \\ 0 & x < 0 \end{cases} \tag{11}$$

The constitutive law for an element subjected to multiaxial stresses can be obtained by substituting the equivalent strain $\bar{\varepsilon}$ for the strain ε in Eqs. (8) and (9). The damage variable then becomes (Wang et al. 2011, 2012a):

$$D = \begin{cases} 0 & \bar{\varepsilon} < \varepsilon_{t0} \\ 1 - \frac{\lambda \varepsilon_{t0}}{\bar{\varepsilon}} & \varepsilon_{t0} \le \bar{\varepsilon} \le \varepsilon_{tu} \\ 1 & \bar{\varepsilon} > \varepsilon_{tu} \end{cases} \tag{12}$$

In the shear failure mode, the damage variable D can be described as follows (Wang et al. 2012b):

$$D = \begin{cases} 0 & \bar{\varepsilon} < \varepsilon_{c0} \\ 1 - \frac{\sigma_{rc}}{E_0 \bar{\varepsilon}} & \bar{\varepsilon} \ge \varepsilon_{c0} \end{cases} \tag{13}$$

where σ_{rc} is the peak strength of the element subjected to uniaxial compression and σ_{c0} is the compressive stress at the point of shear failure.

In addition, the failure (or damage) in every element is assumed to be the source of an acoustic event because the failed element must release its elastic energy stored during the deformation. Therefore, by recording the number of damaged elements and the associated amount of energy release, RFPA3D is capable of simulating acoustic emission (AE) activities, including the AE event rate, magnitude and location. The accumulative damage, D is calculated using the following equation:

$$D = \frac{1}{N} \sum_{i=1}^{s} n_i \tag{14}$$

where s is the number of calculation steps, n_i is the damaged elements in the ith step, and N is the total number of elements in the model (Tang et al. 2007).

In RFPA3D, the specified displacement (or load) is applied to the specimen incrementally. If some elements are damaged in a particular step, their reduced elastic modulus at each stress or strain level is calculated using the above damage variable D as well as Eq. (7). The calculation is then restarted under the current boundary and loading conditions to redistribute the stresses in the specimen until no new damage occurs. Finally, the external load (or displacement) is increased and is used as input for the next step of the analysis. Therefore, the progressive failure process of a brittle material subjected to gradually increasing static loading can be simulated. A user-friendly pre- and post-processor is integrated in RFPA3D to prepare the input data and display the numerical results (Liang et al. 2012).

3 Numerical Model Setup

Figure 3 shows the numerical model. The size of the specimens matches those in the experimental tests of Erarslan and Williams (2012b), with the radius (R) and thickness (t) of the cylindrical specimen both being 26 mm. Figure 4 shows the numerical model for a diametrically loaded disc with a hole. The radius of the disc (R) is 26 mm while, initially, its thickness (t) is 5.2 mm and the radius of

the hole (r) is also 5.2 mm. The latter quantities, as well as the eccentricity (e) of the hole, are also varied to study their influence on the evolution of fracture inside the disc. The specimens in Figs. 3 and 4 were meshed using $3.14 \times 602 \times 10 = 113{,}040$ elements and $3.14 \times (602 - 102) \times 10 = 109{,}900$ elements, respectively. Figure 3 shows the 3D hexahedral element distribution in the numerical model. The basic properties of the rock and steel platens are presented in Table 1 (Erarslan and Williams 2012b). To obtain the overall stress–strain response, a displacement control of 0.002 mm per step was applied axially to the top platen while the bottom platen was fixed.

4 Numerical Results and Discussions

4.1 Numerically Simulated Standard Brazilian Disc Tests

Figure 5 shows the numerically predicted crack evolution during the failure of a Brazilian disc. The left figures show the maximum principal stress distribution, while the right figures show the AE distribution with red and blue circles indicating shear and tensile failure of the elements. Figure 6 compares the predicted stress–strain curve with the stress–strain curve obtained from laboratory experiments (Erarslan and Williams (2012b)).

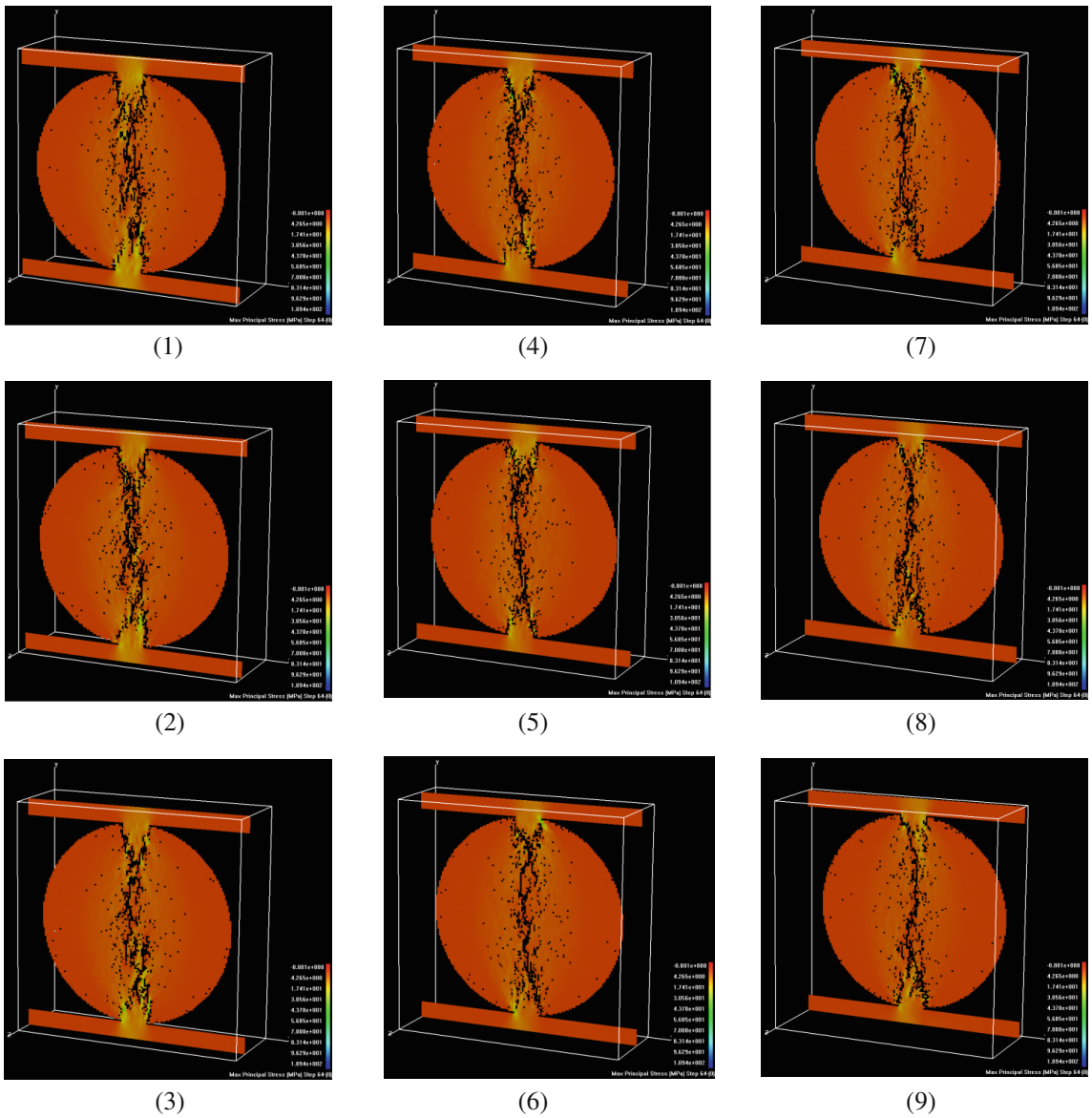

Fig. 9 Numerically simulated failure modes for Brazilian disc divided into nine slices of equal thickness, from front to the back, at the peak stress point D in Fig. 5

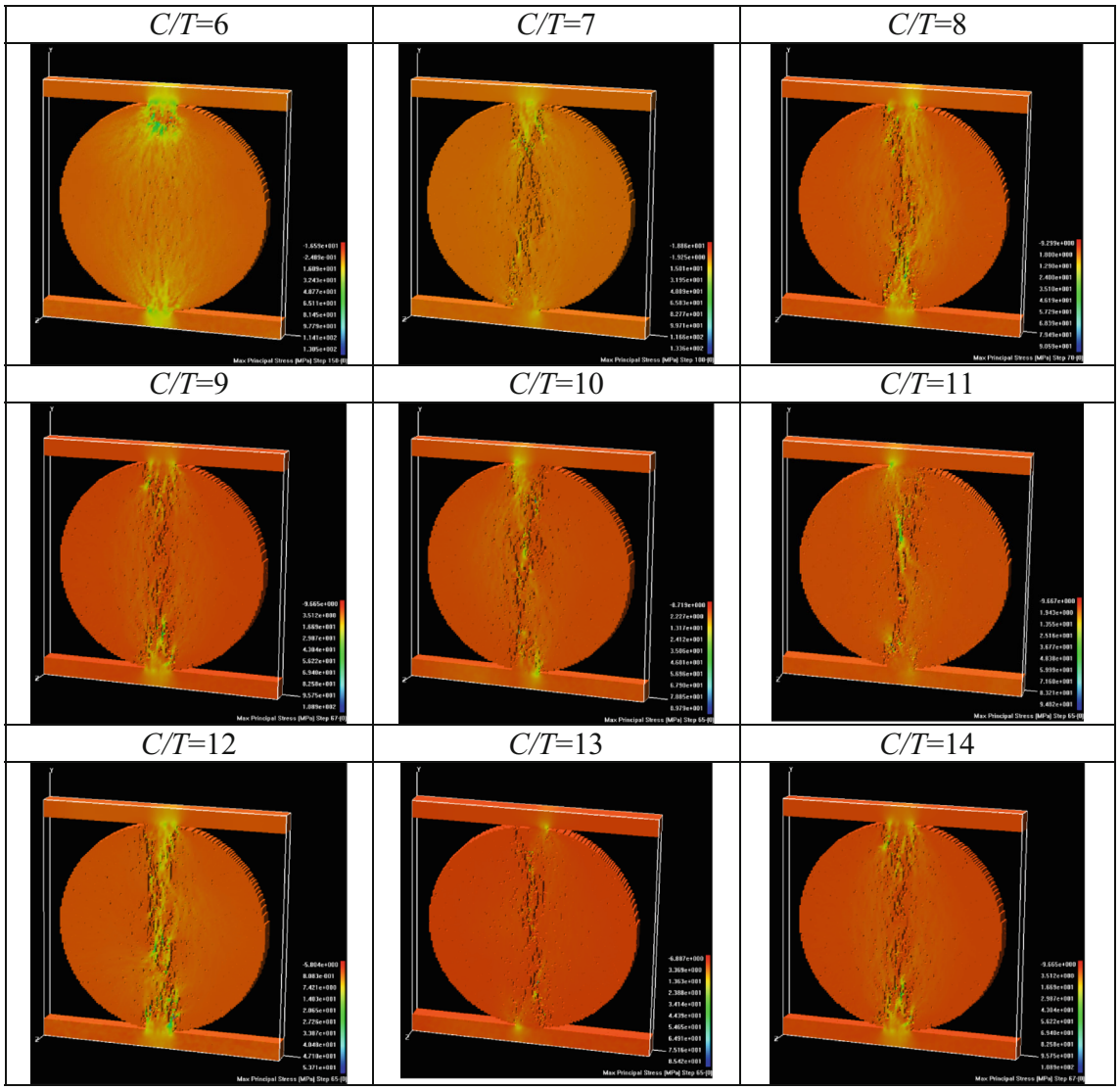

Fig. 10 3D numerically simulated failure modes of Brazilian rock disc for different ratios of compressive strength to tensile strength (*C*/*T*)

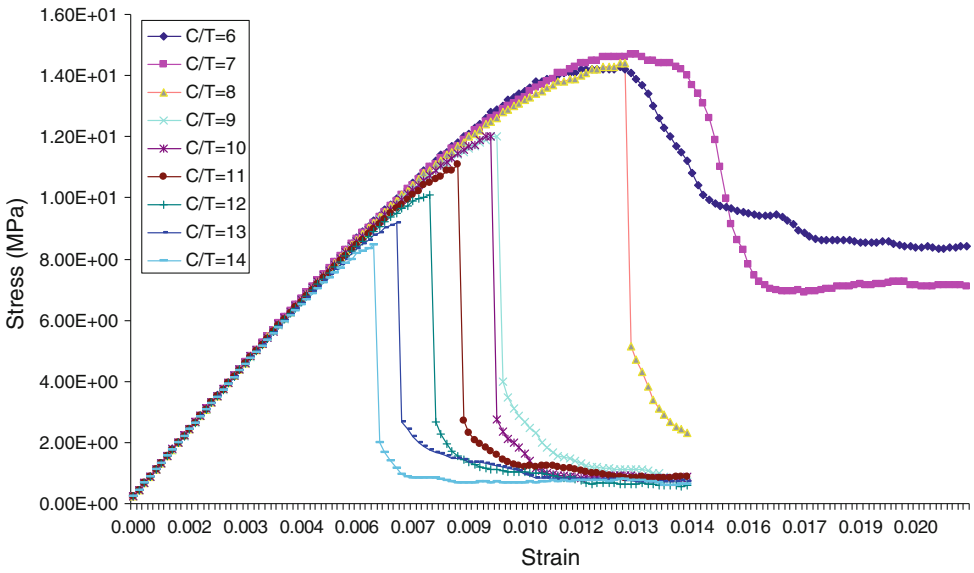

Fig. 11 3D numerically simulated stress–strain curves for different ratios of compressive strength to tensile strength (*C*/*T*)

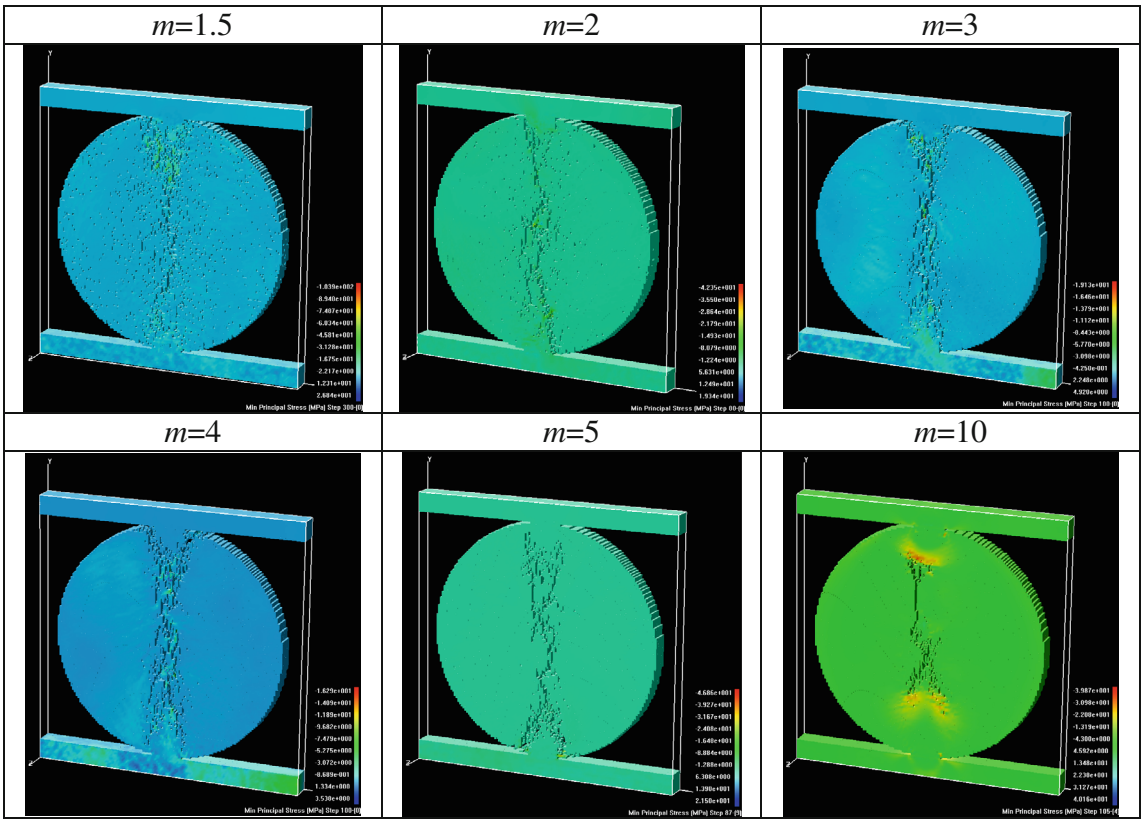

Fig. 12 3D numerically simulated failure modes for Brazilian rock discs with different homogeneity indices (m)

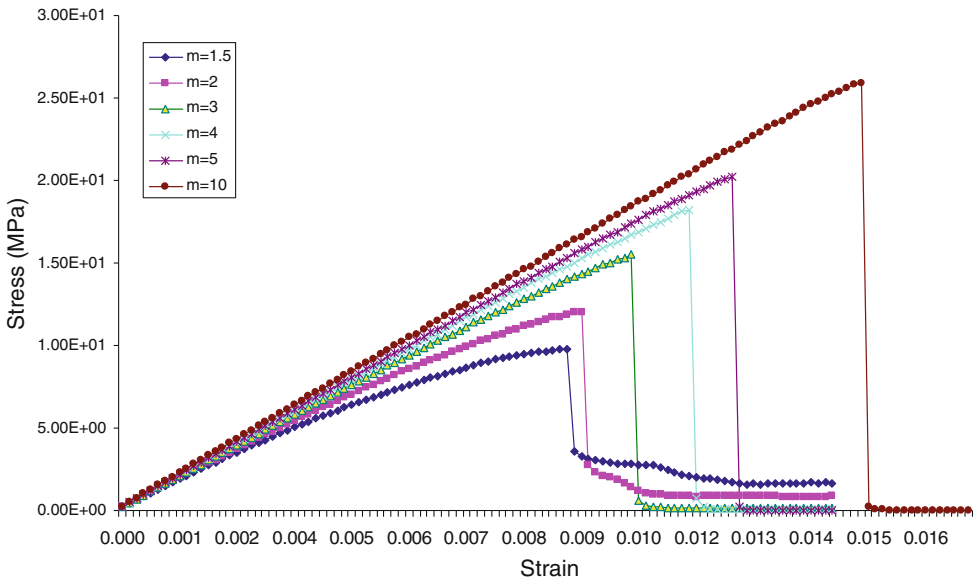

Fig. 13 3D numerically simulated stress–strain curves for specimens with different homogeneity indices (m)

Figure 6 shows that the stress–strain curve is almost linear up to the peak stress level (Point D). Not until Point A (20 % of peak stress), did micro-cracks occur in the simulation (Fig. 5a). During this stage, very few tensile cracks are observed around the vertical diameter of the disc, but shear cracks occur near the loading platens (see red circles in right AE figures). As the uniaxial loading increases to 60 % of peak stress, more micro-tensile cracks are observed but these are concentrated in a narrow zone around the vertical diameter of the disc (see the blue circles in right AE figures). When the stress level reaches 80 % of the peak stress, many of the micro-cracks have coalesced to

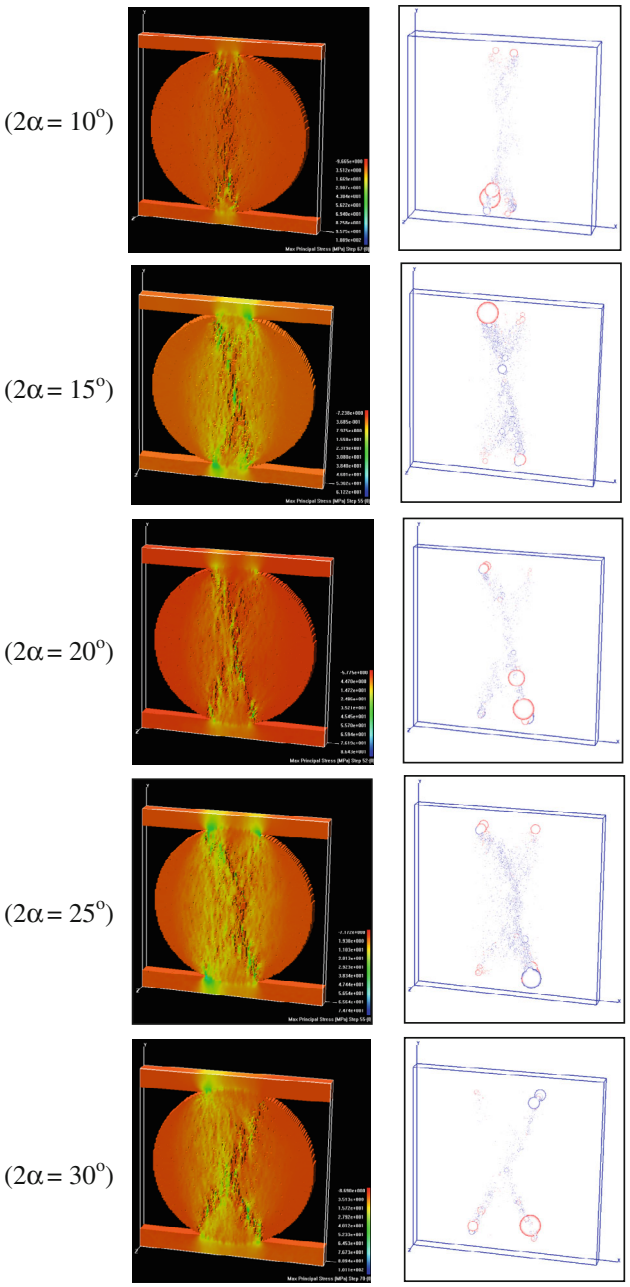

Fig. 14 3D numerically simulated failure modes of Brazilian rock discs with different loading arc angles (2α)

form longer cracks. It is interesting to note that there is one shear crack occurring among many tensile cracks in the AE figure. This is caused by the rock bridge being damaged between the bigger tensile cracks. When the stress level passes the peak stress, Fig. 6 shows that the stress–strain curve drops suddenly to Point E, causing a rapid increase in AE events as illustrated in Fig. 7. Examining Fig. 5d, e, we see that a major crack is formed, which shows good qualitative agreement with the fracture paths observed in the laboratory results (see Fig. 8) of Erarslan and Williams (2012b).

Figure 6 indicates that the numerically predicted peak stress is almost the same as the observed test result, though the post-peak responses are different. Though the numerical simulation gives a sudden drop in the stress–strain response, just like the experimental observation, it underestimates the residual strength. This is possibly due to the choice of input parameters for the numerical model, such as the ratio of the compressive strength to the tensile strength or the homogeneity index (m). The effects of these parameters will be discussed later in the paper. Figure 9 shows the numerical failure modes, along nine slices of equal thickness through the specimen, at the peak stress point D in Fig. 5. This shows that the main crack is not the same in different slices due to the heterogeneity of the rock, so that the failure mode is not symmetrical through the thickness of the specimen.

Figure 10 shows the numerical failure modes of a Brazilian rock disc for different ratios of the compressive (C) and tensile (T) strengths of the rock, while Fig. 11 illustrates the corresponding stress–strain curves. From the latter, we see that the peak stress increases gradually with decreasing values of C/T, while the corresponding strain at the peak stress also increases when $C/T > 7$. This is because with a decrease in C/T, the mean tensile strength increases although the mean compressive strength of the elements remains the same. It is important to note, however, that the mean tensile strength is also much lower than the mean compressive strength, and hence failure of the specimen is mainly caused by tensile damage to the elements. When C/T is less than or equal to 7, the post-peak stress–strain curves show obvious softening, without the brittle type of failure shown for the other cases where $C/T \geq 8$. Consequently, the residual strengths for the samples with $C/T \leq 7$ are much higher than those with $C/T \geq 8$, while the residual strengths are almost the same when $C/T \geq 9$. Interestingly, when $C/T = 6$, the peak stress is lower than that when $C/T = 7$, but the residual strength is higher. This can be explained by examining Fig. 10, which shows that the failure mode for these cases is very different from that of the other samples. Only a few micro-cracks occur around the vertical diameter of the disc, with most of the fractures appearing in the vicinity of the loading platens. The final failure is not dominated by tensile splitting, and is comprised chiefly of compressive/shear cracking. This suggests that the Brazilian test should not be used to determine the tensile strengths for rocks when the ratio of C/T is low.

Figure 12 shows the numerically predicted failure modes for Brazilian tests on samples with various homogeneity indices (m). For a low homogeneity index of $m = 1.5$, many micro-cracks are observed around the major macro-crack which develops along the diameter of the disc. With increasing values of m, which correspond to

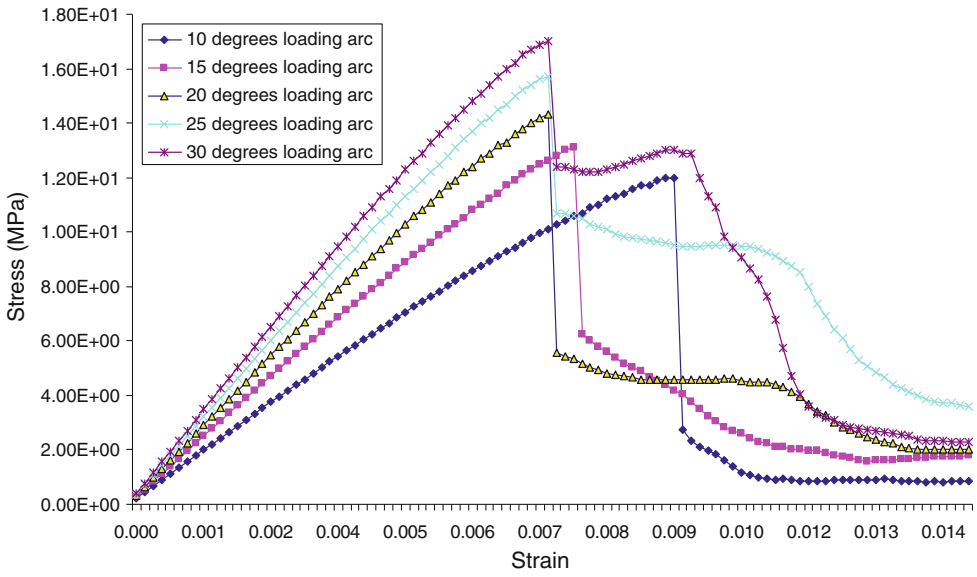

Fig. 15 3D numerically simulated stress–strain curves for Brazilian rock discs with different loading arc angles (2α)

more homogeneous samples, fewer micro-cracks occur around the main macro-crack. From Fig. 13, which shows the stress–strain curves for various values of m, we see that the peak stress increases gradually as m increases. For example, when m is set equal to 1.5, 2, and 3, the respective peak stresses are 9.81, 12.00 and 15.50 MPa. The associated residual strengths for these cases, however, decrease and is equal to 1.67, 0.87 and 0.14 MPa. Interestingly, for the samples with m equal to 4, 5 and 10, the residual strengths are close to zero, which indicates that the Brazilian disc has split in two.

Figure 14 shows the numerically simulated failure modes for Brazilian rock tests with different loading arc angles (2α). As shown in Fig. 1, α is the half central angle of the applied distributed load which is applied using curved platens. A, B, C, and D are the four contact points between the curved platens and the disc. Figure 15 shows the numerically simulated stress–strain curves for various loading arc angles, ranging from 10° to 30°. From this figure, we see that the peak stress increases with increasing loading arc angle, which agrees with the experimental observations of Erarslan and Williams (2012a). For relatively low values of 2α, such as 10° to 15°, the stress–strain response is quite brittle with a rapid drop off after the peak stress has been passed. For values of $2\alpha \geq 20°$, the post-peak response shows a secondary plateau prior to reaching the residual strength. This can be explained by noting that the stresses concentrate at the four contact points A, B, C and D shown in Fig. 1. Although tensile cracks usually start at the centre of the disc and then propagate along the vertical loading diameter, they veer towards these four contact points as they approach the loading platens (Fig. 14). For lower loading arc angles of 10° and 15°, there is only one major fracture to split the sample and the response is therefore quite brittle. However, for higher loading arc angles, greater than or equal to 20°, one major macro-crack typically connects the diagonal A–O–D or B–O–C, and then connects O–C or O–D. This generates a plateau in the sample strength, prior to reaching the residual strength.

Figure 16 shows the numerically predicted failure modes for various sample thicknesses, represented by the normalized ratio (t/R). Figure 17 shows the corresponding stress–strain curves. From Fig. 17, we see that the peak stresses and residual strengths are almost the same for values of t/R of 0.2, 0.4, 0.6, 0.8 and 1, respectively. Theoretically, the controlling stresses are the same for plane stress and plane strain, so that there is no explicit restriction on specimen thickness (Mellor and Hawkes 1971). However, considering the heterogeneity of rock and the probable local stress concentration, the stress distribution will not be uniform along the compressed diameter (Yu et al. 2006). This numerical result agrees with the experimental and numerical results of Yu et al. (2006) who considered cases with $t/R < 0.5$, i.e. for specimens with a low ratio ($t/R < 1$) the stress distribution mostly accords with the theoretical solution (see Eq. 1). The dominant mode of failure for the five cases above, shown in Fig. 16, involves splitting along the loaded diameter. This suggests that the thickness of the sample in a Brazilian test does not have a substantial effect on the failure mode and the inferred tensile strength when the normalized thickness ratio (t/R) <1. The situation for cases with much higher ratios will be discussed in a separate paper.

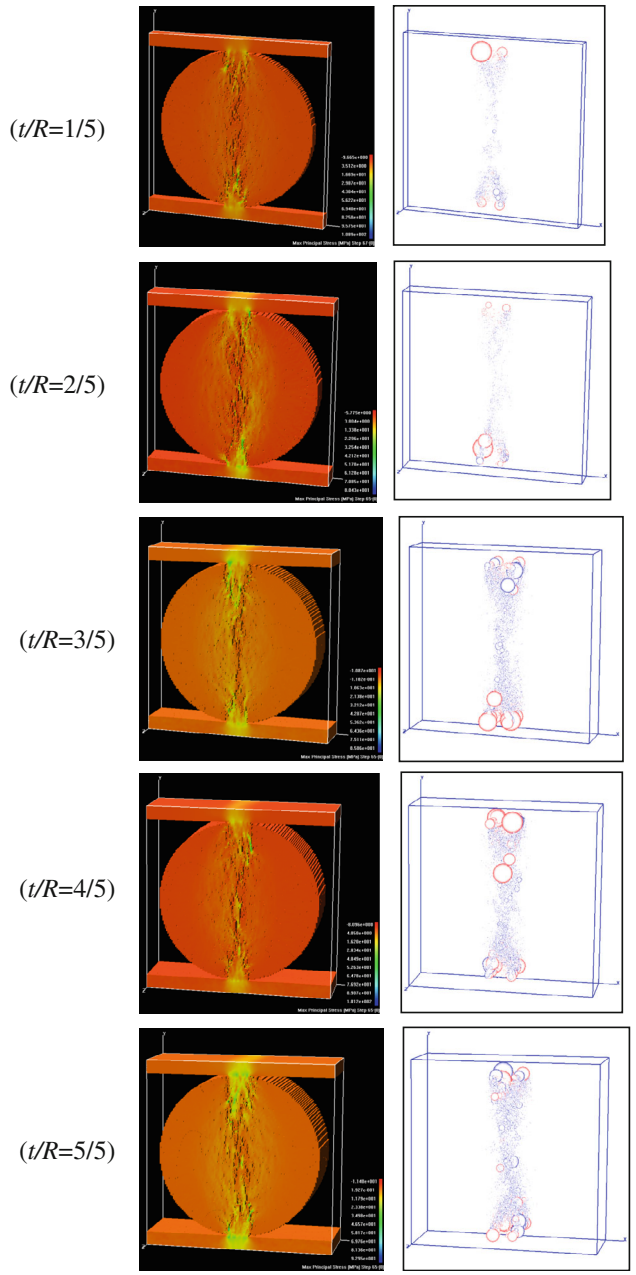

Fig. 16 3D numerically simulated failure modes for different normalized thickness of disc (t/R) (R is the radius of disc)

4.2 Numerically Simulated Failure Mechanism of a Disc with a Central Hole

The aim of this section is to gain a better insight into the failure mechanism of a disc with a central hole, subjected to diametric compression. The geometry of the ring specimen and the loading conditions are given in Fig. 2. To study the effect of the size of the hole, the ratio of the internal to external radius, r/R, is taken as 0.083, 0.167, 0.25, 0.333, 0.417 and 0.5. The Weibull distribution parameters for the numerical tests are the same as those for Brazilian specimens, and are listed in Table 1.

Figure 18 shows the numerically simulated failure patterns for a rock disc with a hole in the centre and $r/R = 0.33$, $m = 2$, $2\alpha = 10°$ and $t/R = 0.4$. Figure 19 is the corresponding stress–strain curve with a comparison of that to a disc without a hole. Stages A–H in Fig. 18 are related to the points A–H in the stress–strain curve in Fig. 19. Firstly, we note that, due to the existence of the central hole, the peak stress of the ring specimen is much lower than that of the disc specimen. At Stage A in Fig. 18, when the vertical applied strain is 0.002, primary cracks are observed near the top and bottom walls of the hole. As the loading is increased, these primary cracks propagate along the loading diameter toward the loading platens (see Stage B). However, these primary cracks cease to propagate when they reach the contact zone between the platen and the sample at a vertical strain of 0.004 (Stage C). Stage C corresponds to the peak point C in the stress–strain curve in Fig. 19, and precedes the propagation of secondary tensile cracks along the horizontal diameter towards the surface of the central hole (Stage D). When the strain reaches 0.0059, these secondary cracks reach the edge of the central hole and the right half of the ring loses most of its capacity to bear load. This causes the load to be transferred to the left half of the sample which, in turn, results in the formation of cracks along the radius that propagate toward the surface of the internal hole (See Stage F). Stage F corresponds to the second peak stress point F in Fig. 19. Increasing the applied load from points F to G causes another drop in stress–strain response, indicating that the left half of the sample has also lost its capacity to bear load. Finally, the specimen splits into four parts after reaching its residual load capacity (Stage H). Overall, although the input geometrical and material properties in Table 1 are not completely the same as those in the laboratory tests of Mellor and Hawkes (1971), the numerical simulations capture well the typical failure patterns that are observed in the laboratory tests, which are shown in the first row in Fig. 20. This Figure shows that as the diameter of the hole is decreased, secondary cracks are not observed along the horizontal diameter. The effect of the diameter of the hole on the failure modes and the peak stress of the specimen are discussed in the next paragraph.

Figure 21 shows the numerically predicted failure modes of ring specimens with holes of various sizes, as measured by the dimensionless quantity r/R. Figure 22 shows the corresponding stress–strain curves. From Fig. 21, we see that when $r/R \leq 0.25$, only a single vertical micro-cracking zone is formed which passes through the central hole and eventually splits the specimen. However, when r/R is higher such as 0.333, 0.417 and 0.5, second cracks are observed and the specimen is divided into four

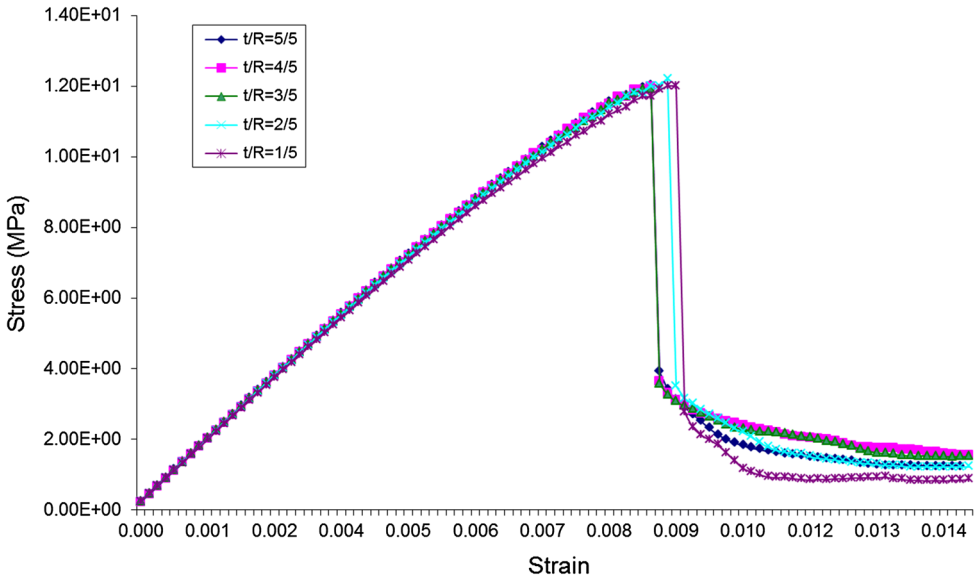

Fig. 17 3D numerically simulated stress–strain curves for different normalized thickness of disc (t/R)

parts. It is noted that due to the heterogeneity of the rock, these cracks are not completely aligned along the horizontal diameter of the specimen. From Fig. 22, it is clear that the peak stress decreases with the increasing values of r/R. For the three cases with r/R being 0.083, 0.167 and 0.25, respectively, there is an obvious stress drop after the first peak stress, but there is not a subsequent stress drop because secondary cracking does not occur. For the other three cases of $r/R = 0.333$, 0.417 and 0.5, there is no clearly defined stress drop after the first peak stress but, instead, a distinct stress drop after the second peak stress is reached. This is caused by the occurrence of secondary cracking in these three cases.

4.3 Numerically Simulated Failure Mechanism of a Disc with an Eccentric Hole

Figures 23 and 24 show the experimental results for a diametrically loaded disc with an eccentric hole of two different radii (Van de Steen et al. 2005). Figure 23 shows that for the case with a small hole and eccentricity, failure occurs by splitting along the diameter without intersecting the hole. In contrast, for a sample with a larger hole and the same eccentricity, shown in Fig. 24, two primary cracks intersect the hole from the top and bottom platens. However, in these experimental tests, the effect of the eccentricity on the failure mode of the specimens was not considered. Therefore, in this section, the effects of both the radius and eccentricity of the hole will be simulated numerically.

Figure 25 shows the numerically simulated failure process of a rock disc with an eccentric hole. In this case, the normalized horizontal eccentricity is $e/R = 0.333$, $r/R = 0.167$, $m = 2$, $2\alpha = 10$, and $t/R = 0.4$. Figure 26 shows the corresponding stress–strain curve with a comparison of results for a disc without a hole. As expected the peak stress for the sample with an eccentric hole is much lower than that of a standard disc specimen. The points A–H in Fig. 26 correspond to the stages A–H in Fig. 25. From the latter figure we see that when the vertical applied strain is 0.002 (stage A), two primary cracks are initiated from the surface of the hole and propagate towards the top and bottom loading platens. When the strain is 0.004 (Stage C), these primary cracks cease to grow, but two secondary cracks initiate in the vicinity of the top and bottom platens. From Stages C to E, these two secondary cracks start to propagate towards the top and bottom contact zones between the platens and the disc. Simultaneously, the primary cracks also continue to grow, but very slowly, and do not coalesce with the secondary cracks. When the applied vertical strain reaches 0.0066 (Stage F), the secondary cracks coalesce to form a major fracture which bends towards the surface of the eccentric hole. With further loading, a third crack initiates at the right edge of the disc along the horizontal diameter. This horizontal crack eventually propagates to the surface of the hole, but there is no distinct stress drop at the corresponding point H in Fig. 26.

Figure 27 shows the numerically predicted failure modes of specimens with various horizontal hole eccentricities (e/R) of 0, 0.167, 0.333, 0.5, 0.666 and 0.833. Figure 28 shows the corresponding stress–strain curves. When $e/R \leq 0.167$, only two primary cracks reach the hole, while for cases with $e/R = 0.333$ and 0.5, additional secondary cracks form along a line towards the hole as well as along the diameter. For the largest hole eccentricities, failure is caused by primary splitting along the loaded diameter without intersecting the hole. From Fig. 28, we

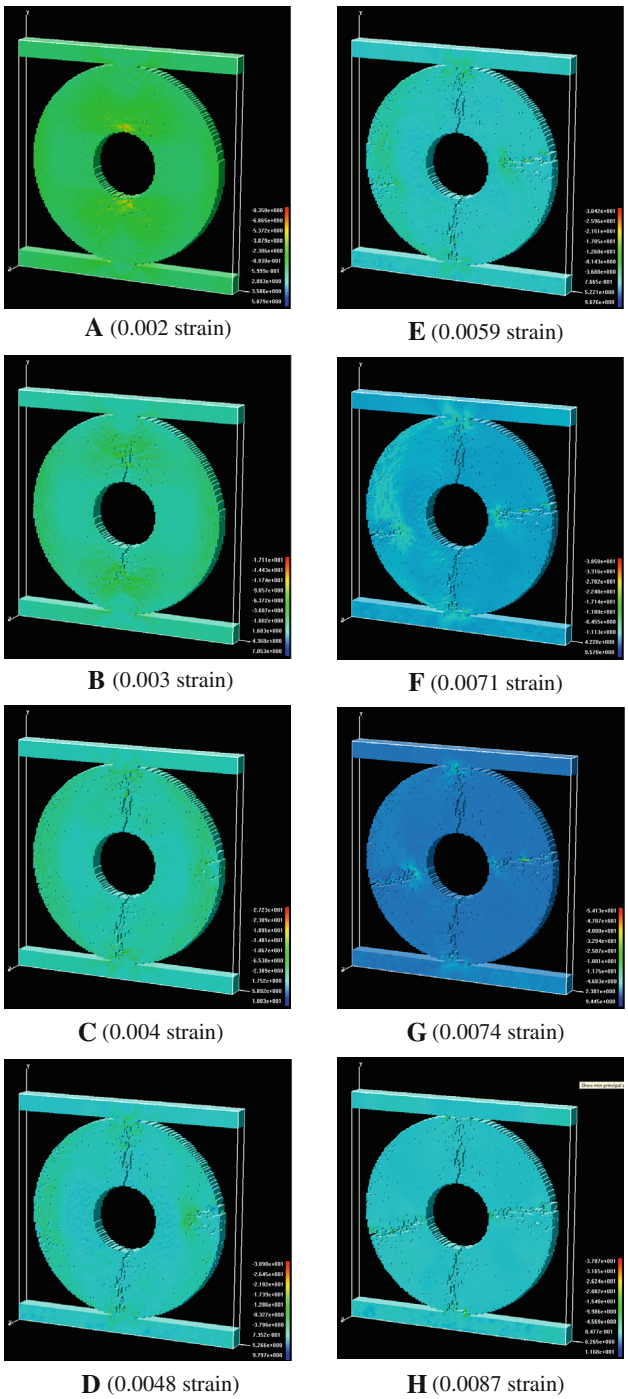

Fig. 18 3D numerically simulated failure process of rock disc with a hole in the center ($e = 0$, $r/R = 0.333$, $m = 2$, $2\alpha = 10$, $t/R = 2/5$) (minimum principal stress distribution)

see that the peak stress increases with an increasing value of eccentricity, with the largest eccentricities resulting in behaviour which is similar to that for a standard Brazilian disc.

Figure 29 shows the numerically predicted failure modes for samples with the same eccentricity but holes of various sizes (r/R). Figure 30 shows the corresponding stress–strain curves. From Fig. 29, we see that for small values of r/R, the tensile cracks forming around the hole do not propagate very far, with the failure mode being very similar to that for a standard Brazilian sample, i.e. splitting of the disc along the loaded diameter. This indicates that when the hole is very small with a moderate eccentricity, it has little influence on the evolution of cracking. However, as the size of the hole is increased, it not only influences the formation and propagation of primary tensile cracks, but also causes secondary cracks that bend out from the loaded diameter. For the case with the largest hole ($r/R = 0.25$), primary cracks initiate from the hole and propagate almost parallel to the loaded diameter. From Fig. 30 we see that, when the eccentricity is the same, the peak stress decreases as the size of the hole increases. This is what we expect on physical grounds.

Figure 31 shows the numerically simulated failure modes for specimens with various values of homogeneity index (m). Figure 32 illustrates the corresponding stress–strain curves. From Fig. 31, we see that more micro-cracks are generated around the major cracks when the homogeneity index is low. Indeed, when $m \leq 1.1$, the major cracks are not distinct. In contrast, when $m \geq 4$, the major cracks are very distinct and almost no micro-cracks are evident. Figure 32 shows that the peak stress decreases gradually as the homogeneity index is increased. For the cases with $m \leq 1.1$, the mode of failure is ductile in nature with no pronounced drop in the stress–strain response after the peak stress has been passed. This suggests that when the material is very heterogeneous, the effect of the hole on the load capacity of the specimen is weaker. In comparison, when $m \geq 2$, there are marked drop-offs in the strength as the applied strain increases, even though the peak strength increases with increasing values of m.

5 Conclusions

The code RFPA^{3D} has been used to study the failure mechanisms of the standard Brazilian disc and discs with a central hole or eccentric hole. The following conclusions can be drawn:

1. The three-dimensional numerical model (RFPA^{3D}) has been validated against the results of standard Brazilian tests performed on Brisbane tuff (Erarslan and Williams 2012b). The numerical model predicts both the failure and the peak stress with acceptable accuracy, and has been used to investigate the influence of the ratio of the compressive strength to tensile strength (C/T), the heterogeneity index (m), and the loading arc angle (2α). As C/T increases from 7 to 14, both the

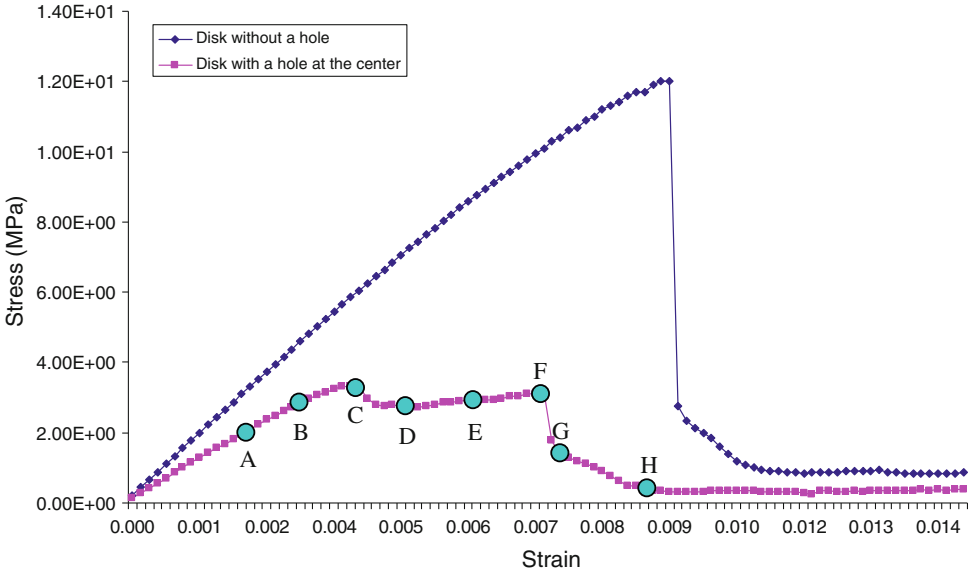

Fig. 19 3D numerically simulated stress–strain curves for rock disc and disc with hole at the centre

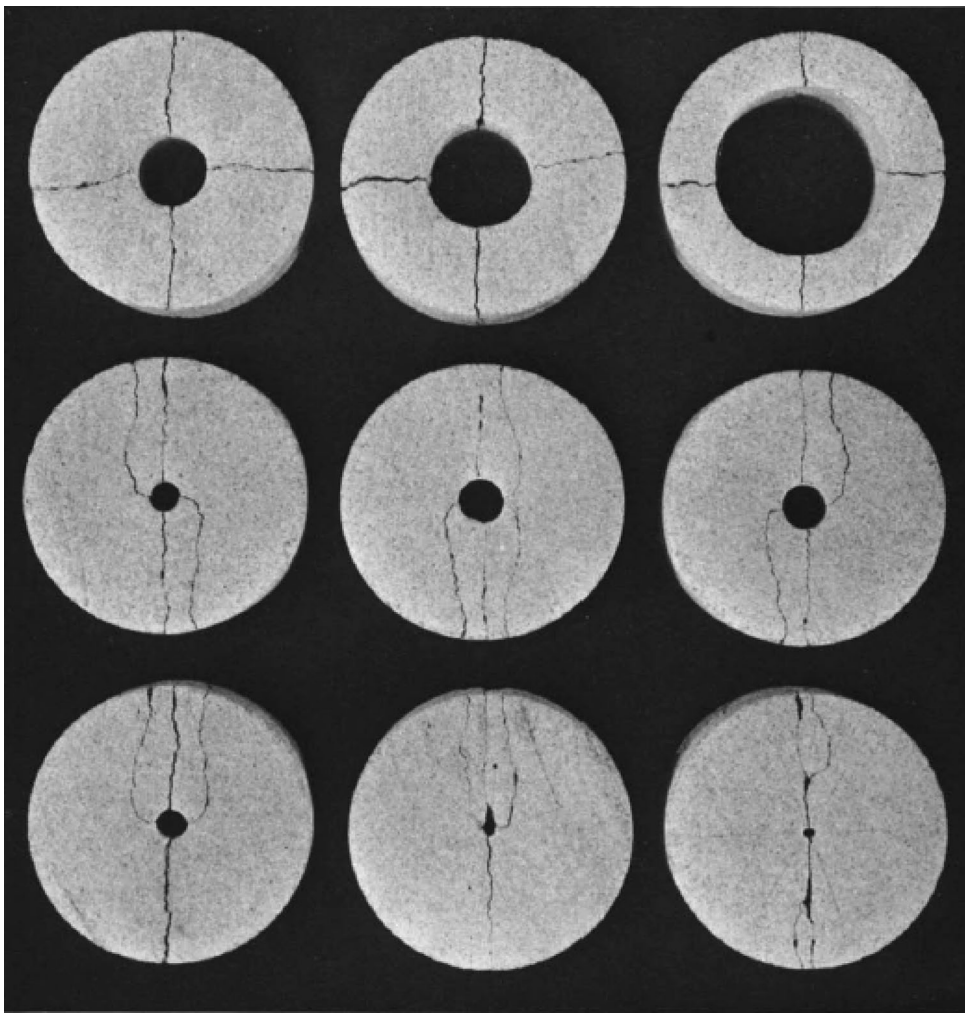

Fig. 20 Experimental results for ring specimens tested by simple methods using flat platens with different ratios of *r*/*R* (Mellor and Hawkes 1971)

peak stress and the residual strength of specimen increase gradually. As *m* is increased from 1.5 to 10, the peak stress of the specimen also increases. This effect is also observed when the loading arc angle is increased from 10° to 30°. Importantly, the thickness of the Brazilian specimen does not appear to have a

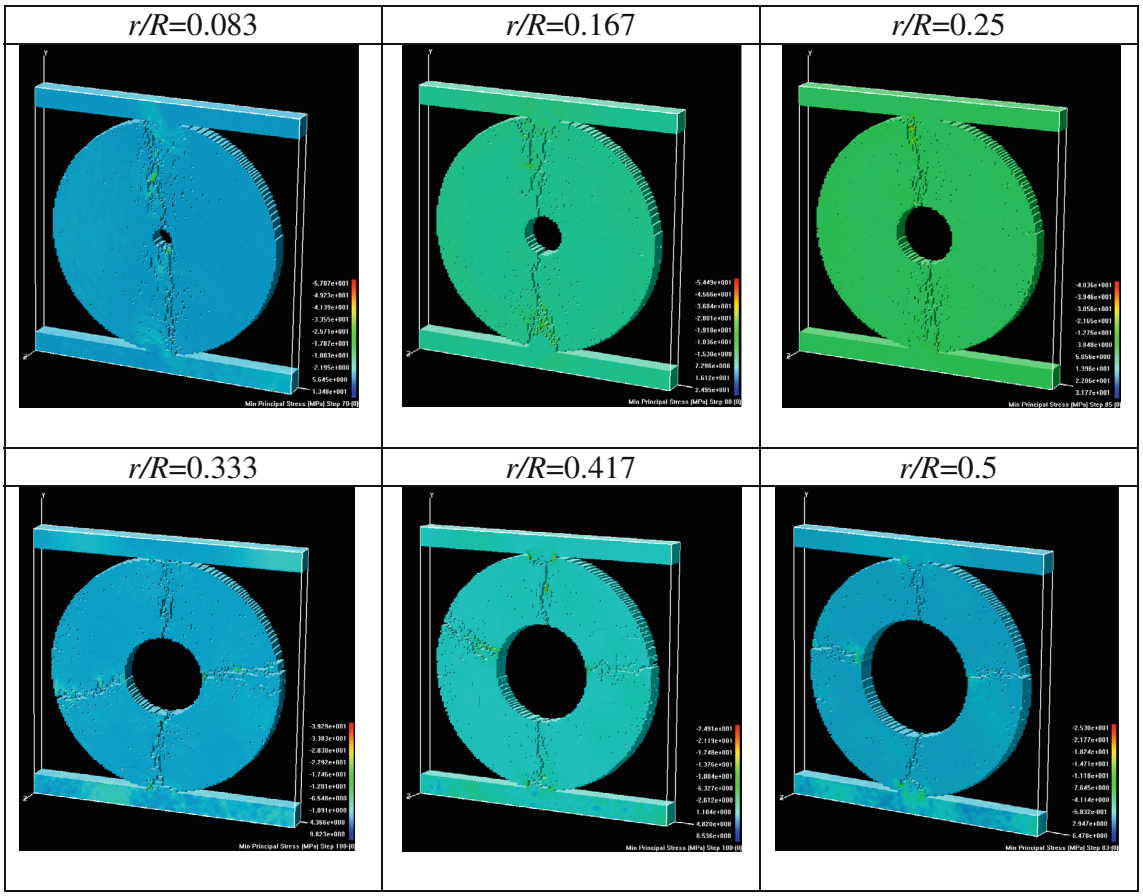

Fig. 21 3D numerically simulated failure modes of ring specimens with different ratios of r/R (r is the radius of the hole, R is radius of the disc)

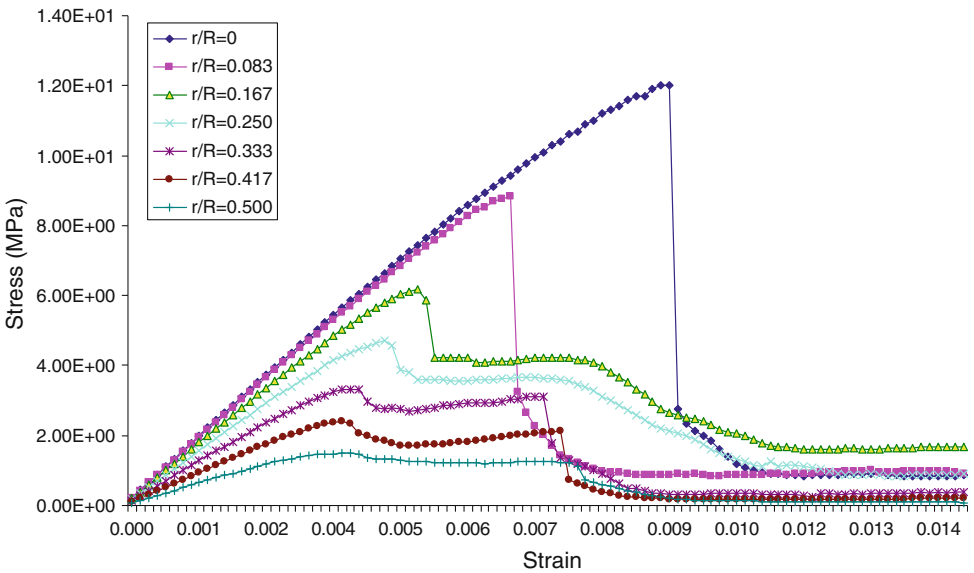

Fig. 22 3D numerically simulated stress–strain curves for specimens with different r/R (r is the radius of the hole, R is radius of the disc)

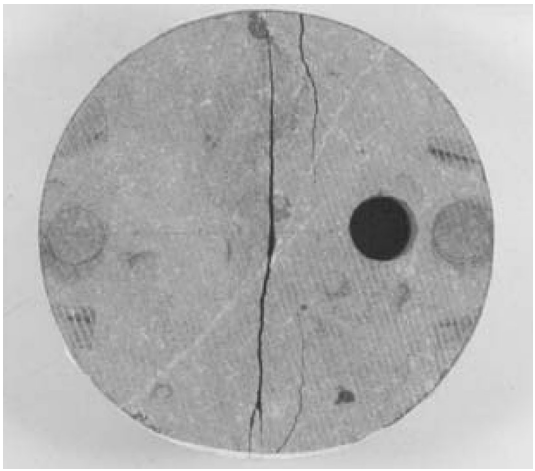

Fig. 23 Observed failure of diametrically loaded disc with a hole, showing split along the diameter without intersecting the hole (Van de Steen et al. 2005)

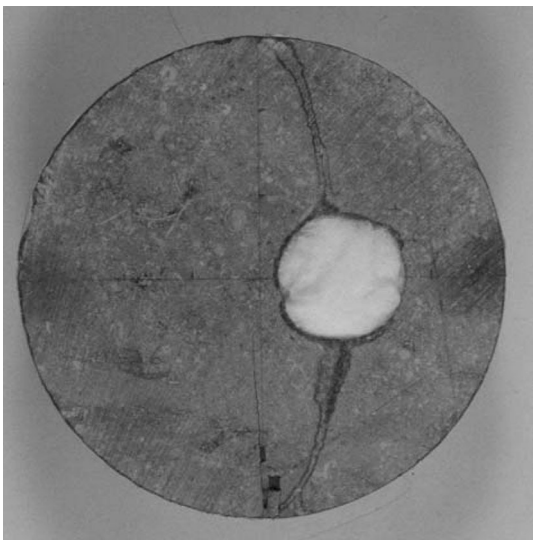

Fig. 24 Observed failure of diametrically loaded disc with a hole, showing primary fractures intersecting the hole and a secondary fracture growing from the bottom platen contact to the centre of the disc (Van de Steen et al. 2005)

marked effect on the failure modes and the peak stress of the specimen when the normalized thickness ratio (t/R) <1.

2. For a disc with a central hole, the numerical model qualitatively reproduces the primary cracks that are observed to propagate along the loaded diameter, with secondary cracks intersecting the hole along the horizontal diameter (Mellor and Hawkes 1971). The numerical results also show that the peak stress of a specimen increases as the normalized hole size is decreased.
3. For the specimens with an eccentric hole, the numerically simulated primary crack patterns broadly agree

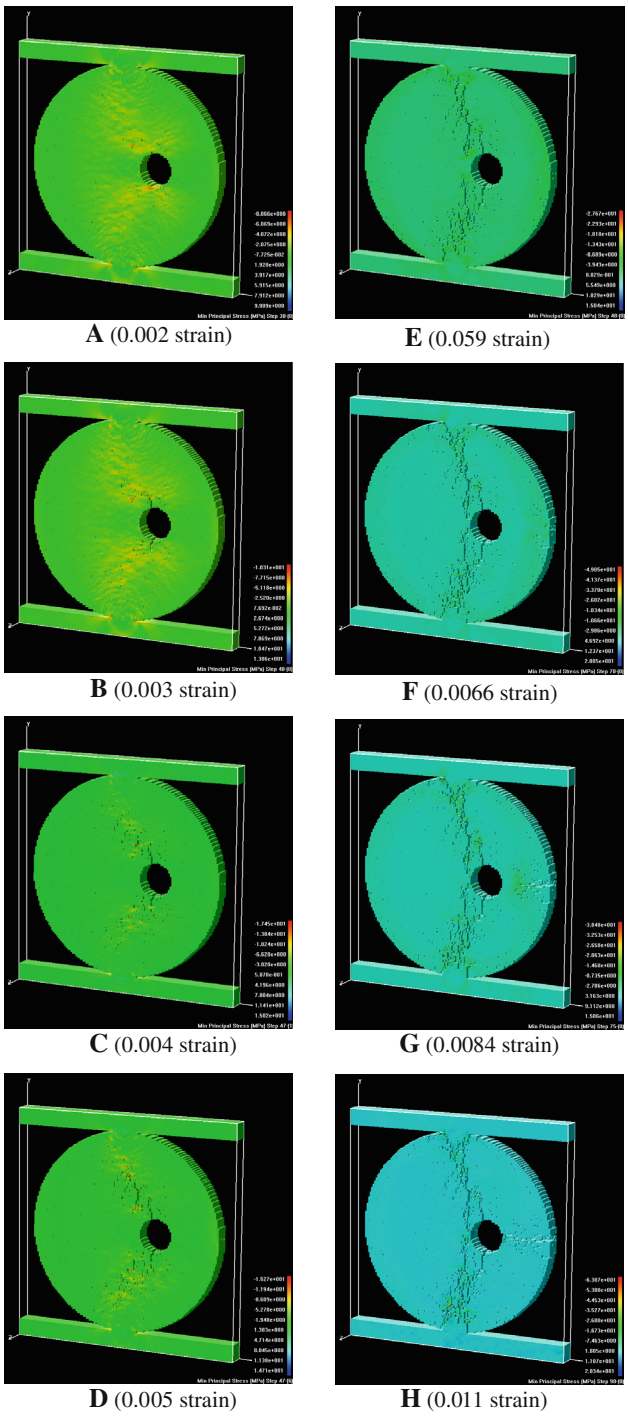

Fig. 25 3D numerically simulated failure process of rock disc with an eccentric hole ($e/R = 0.333$, $r/R = 0.167$, $m = 2$, $2\alpha = 10$, $t/R = 2/5$) (minimum principal stress distribution)

with those observed in laboratory tests (Van de Steen et al. 2005). For a fixed hole size, the peak stresses increases as the horizontal eccentricity (e/R) is increased. Conversely, when the horizontal eccentricity is kept the same, the predicted peak stress decreases as the size of the hole is increased and the failure mode

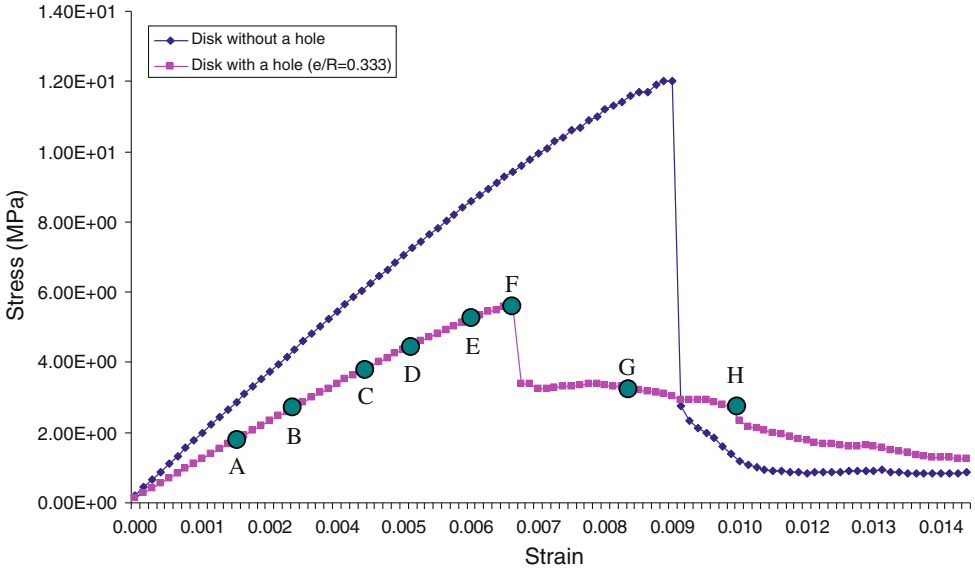

Fig. 26 3D numerically simulated stress–strain curves for rock discs, with and without a hole ($e/R = 0.333$, $r/R = 0.167$, $m = 2$, $2\alpha = 10$, $t/R = 2/5$)

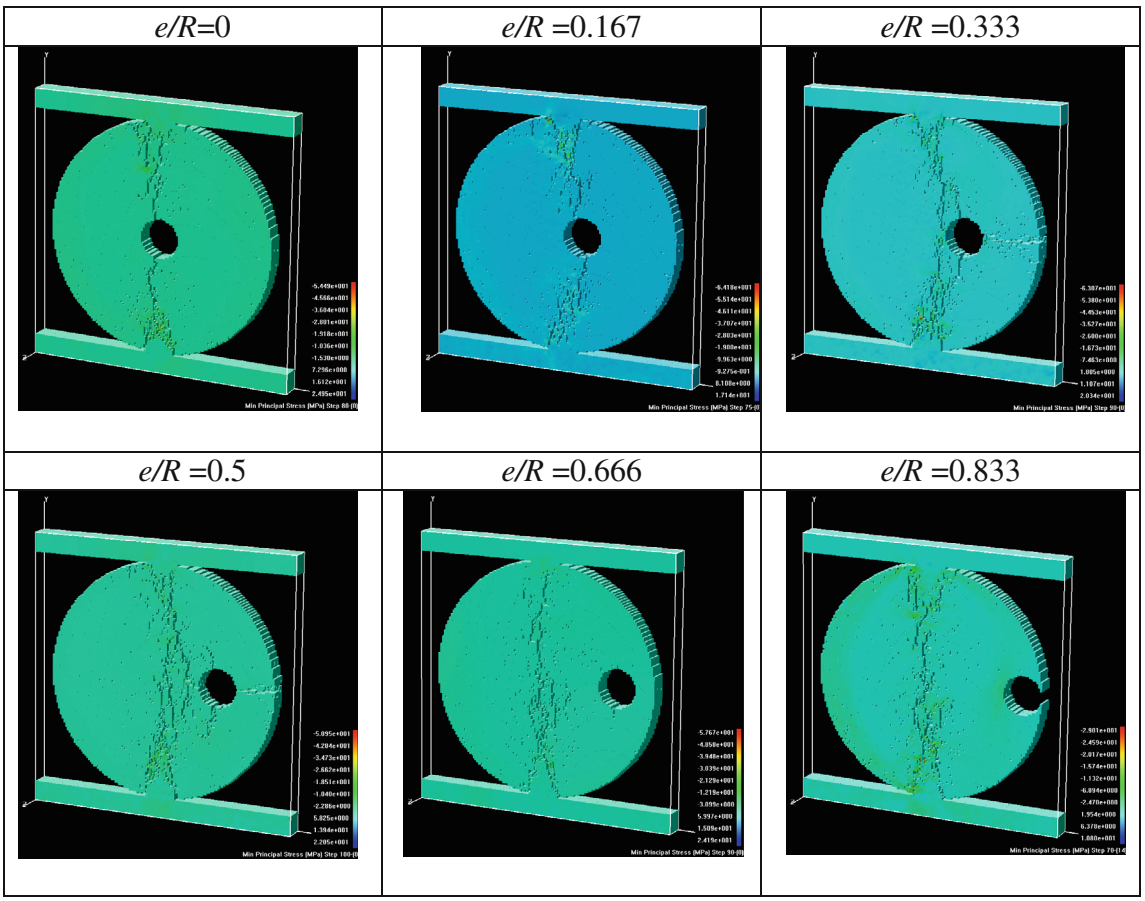

Fig. 27 3D numerically simulated failure modes for specimens with various horizontal hole eccentricities (e/R) ($r/R = 0.167$, $m = 2$, $2\alpha = 10$, $t/R = 0.4$)

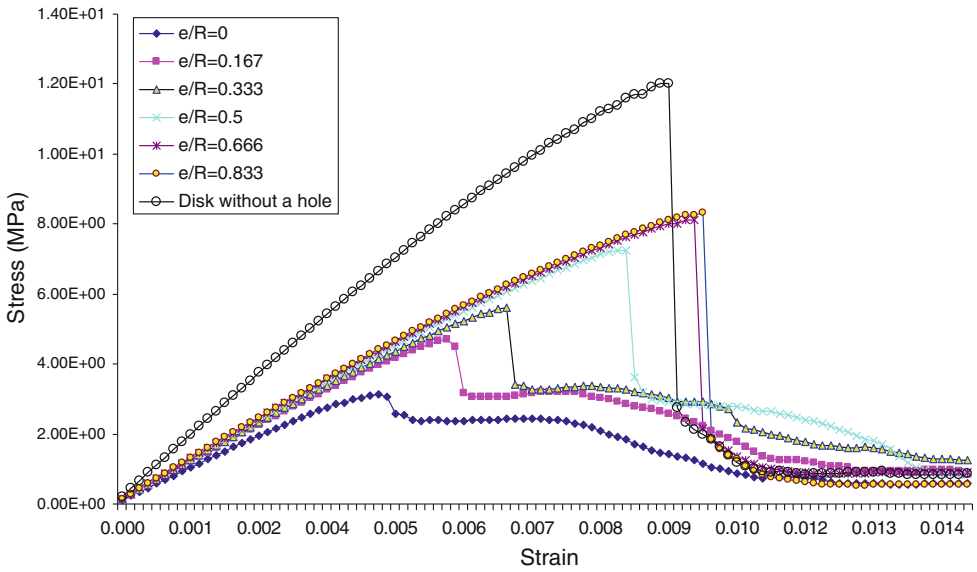

Fig. 28 3D numerically simulated stress–strain curves for specimens with various horizontal hole eccentricities (e/R) ($r/R = 0.167$, $m = 2$, $2\alpha = 10$, $t/R = 0.4$)

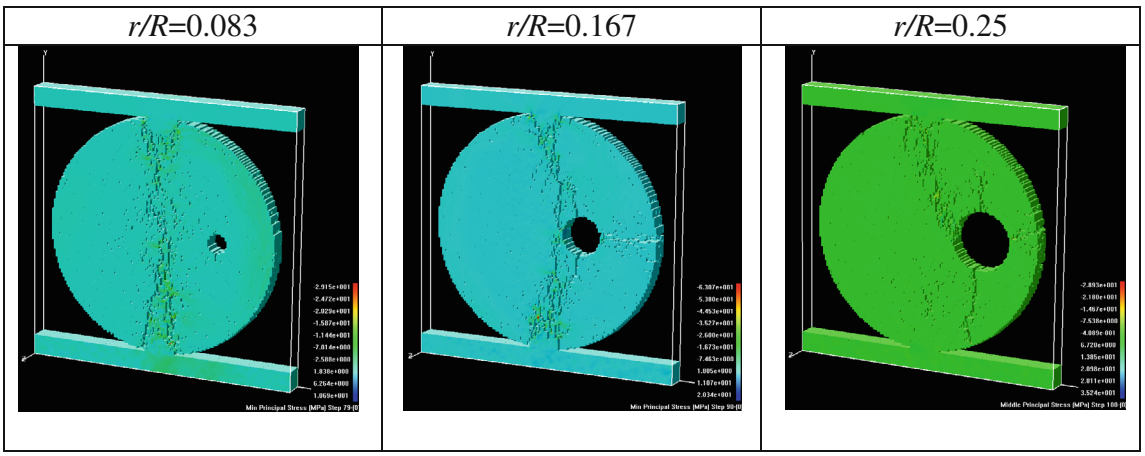

Fig. 29 3D numerically simulated failure modes for specimens with the same horizontal eccentricity ($e/R = 0.333$) but holes of various sizes (r/R) ($m = 2$, $2\alpha = 10$, $t/R = 0.4$)

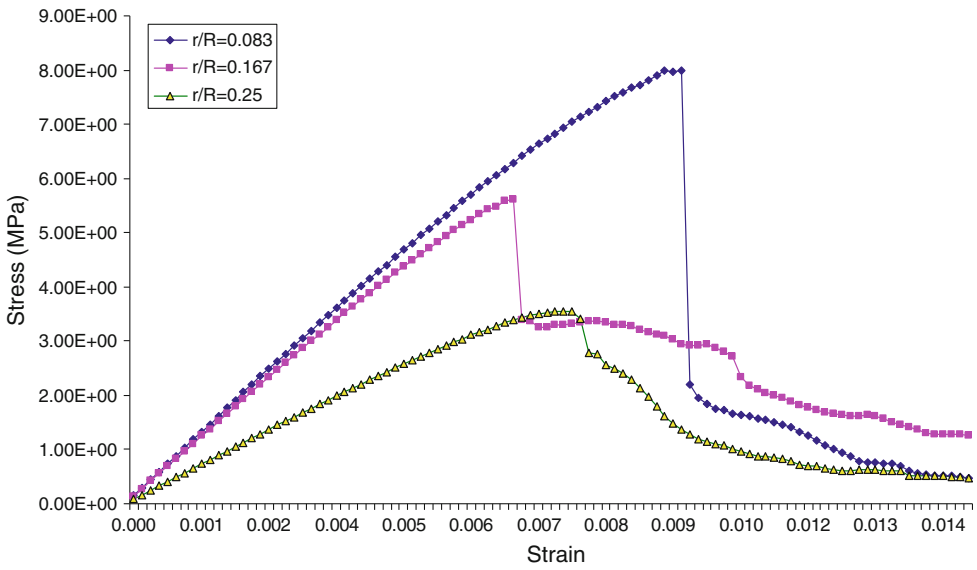

Fig. 30 3D numerically simulated stress–strain curves for specimens with the same horizontal eccentricity ($e/R = 0.333$) but holes of various sizes (r/R) ($m = 2$, $2\alpha = 10$, $t/R = 0.4$)

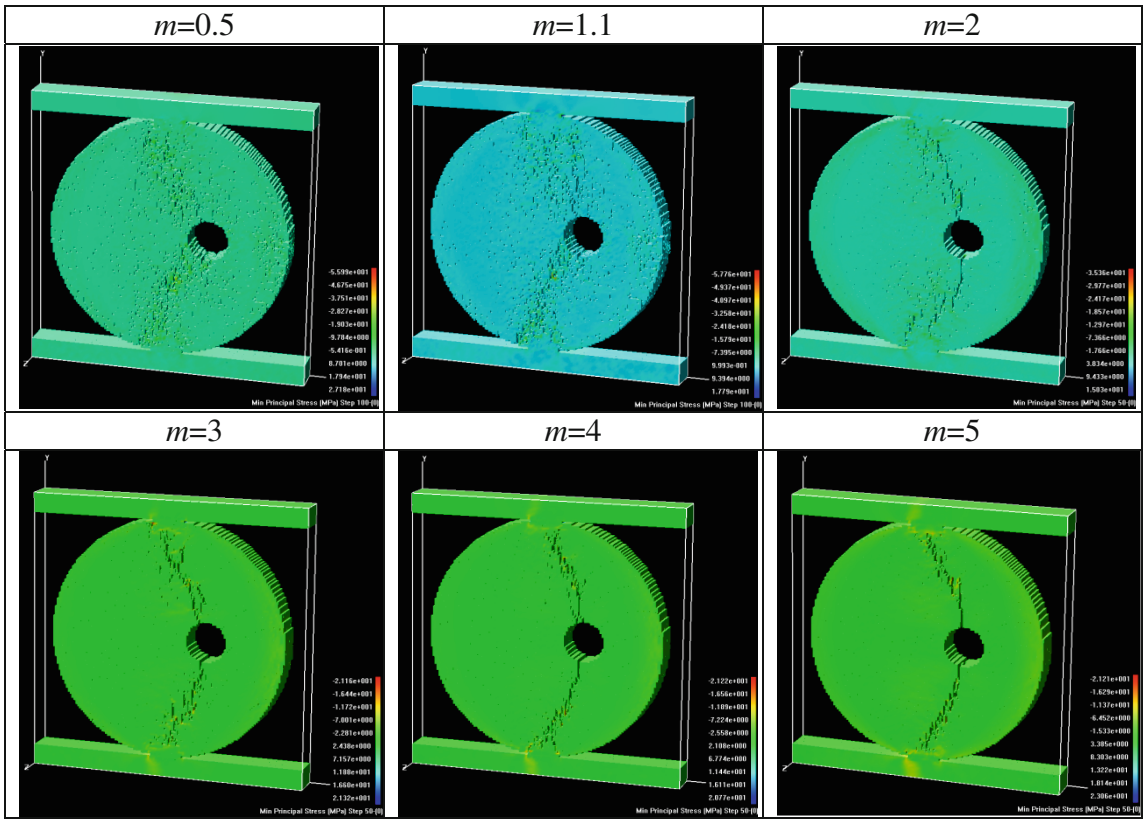

Fig. 31 3D numerically simulated failure modes for specimens with various homogeneity indices (m) ($e/R = 0.333$, $r/R = 0.167$, $m = 2$, $2\alpha = 10$, $b/R = 0.4$)

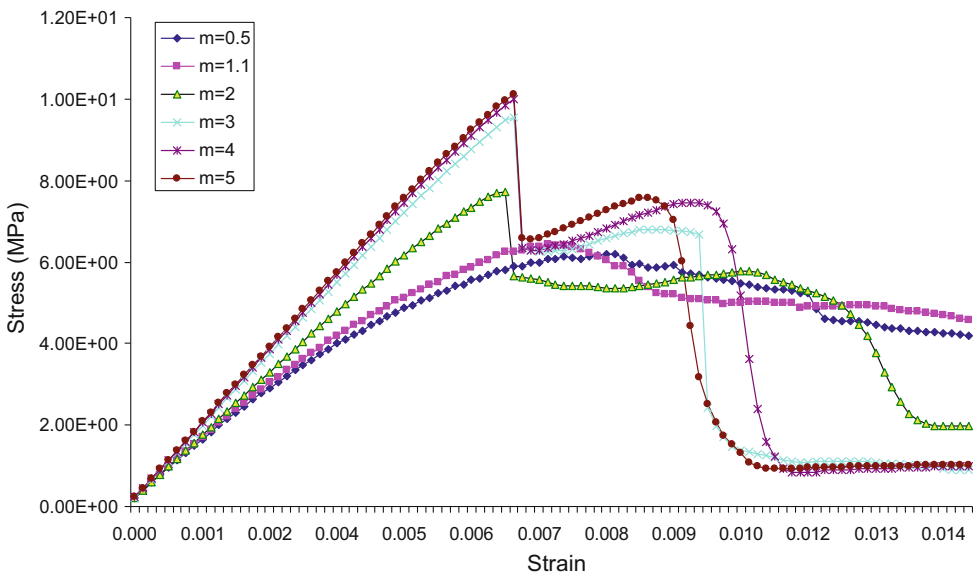

Fig. 32 3D numerically simulated stress–strain curves for specimens with various homogeneity indices (m) ($e/R = 0.333$, $r/R = 0.167$, $m = 2$, $2\alpha = 10$, $t/R = 0.4$)

is also affected. When both the radius and horizontal eccentricity are kept constant, the final crack pattern is much more distinct for a higher homogeneity index (m), while the peak stress also increases as m increases.

Acknowledgments The work described in this paper is partially supported by ARC Australian Laureate Fellowship grant FL0992039 and ARC CoE Early Career Award Grant CE110001009, for which the authors are very grateful.

References

Bahrani N, Potyondy DO, Pierce M (2012) Simulation of Brazilian test using PFC2D grain-based model. In: Proceedings of 21st Canadian rock mechanics symposium, Edmonton

Berenbaum R, Brodie I (1959) Measurement of the tensile strength of brittle materials. Br J Appl Phys 10:281–286

Bieniawski ZT, Hawkes I (1978) Suggested methods for determining tensile strength of rock materials. Int J Rock Mech Min Sci Geomech Abstr 15(3):99–103

Cai M, Kaiser PK (2004) Numerical simulation of the brazilian test and the tensile strength of anisotropic rocks and rocks with pre-existing cracks. Int J Rock Mech Min Sci 41(3), CD-ROM, Paper 2B03-SINOROCK2004 Symposium

Chen CS, Pan E, Amadei B (1998) Fracture mechanics analysis of cracked discs of anisotropic rock using the boundary element method. Int J Rock Mech Min Sci 35(2):195–218

Erarslan N, Williams DJ (2012a) Experimental, numerical and analytical studies on tensile strength of rocks. Int J Rock Mech Min Sci 49:21–30

Erarslan N, Williams DJ (2012b) Investigating the effect of cyclic loading on the indirect tensile strength of rocks. Rock Mech Rock Eng 45(3):327–340

Erarslan N, Liang ZZ, Williams DJ (2012) Experimental and numerical studies on determination of indirect tensile strength of rocks. Rock Mech Rock Eng 45(5):739–751

Fairhurst C (1964) On the validity of the 'Brazilian' test for brittle material. In J Rock Mech Min Sci 1:535–564

Griffith AA (1920) The phenomena of rupture and flow in solids. Philos Trans R Soc Lond A 221:163

Hobbs DW (1964) The tensile strength of rocks. Int J Rock Mech Min Sci 1:385–396

Hobbs DW (1965) An assessment of a technique for determining the tensile strength of rock. Br J Appl Phys 16:259–269

Hudson JA (1969) Tensile strength and the ring test. Int J Rock Mech Min Sci 6:91–97

ISRM (1978) Suggested methods for determining tensile strength of rock materials. Int J Rock Mech Min Sci Geomech Abstr 15:99–103

Jaeger JC, Cook NGW (1979) Fundamentals of rock mechanics. Chapman-Hall and Science, London

Jiao YY, Zhang XL, Zhao J (2012) Two-dimensional DDA contact constitutive model for simulating rock fragmentation. J Eng Mech 138:199–209

Lanaro F, Sato T, Stephansson O (2009) Microcrack modeling of Brazilian tensile tests with the boundary element method. Int J Rock Mech Min Sci 46:450–461

Lavrov A, Vervoort A, Wevers M, Napier JAL (2002) Experimental and numerical study of the Kairser in cyclic Brazilian tests with disc rotation. Int J Rock Mech Min Sci 39(3):287–302

Liang ZZ, Xing H, Wang SY, Williams DJ, Tang CA (2012) A three-dimensional numerical investigation of fracture of rock specimen containing a pre-existing surface flaw. Comput Geotech 45:19–33

Mellor M, Hawkes I (1971) Measurement of tensile strength by diametral compression of discs and annuli. Eng Geol 5:173–225

Ripperger EA, Davids N (1947) Critical stresses in a circular ring. Trans Am Soc Civil Eng 2308:619–635

Sun L, Zhao GF, Zhao J (2013) Particle manifold method (PMM): a new continuum–discontinuum numerical model for geomechanics. Int J Numer Anal Methods Geomech 37:1711–1736

Tang CA (1997) Numerical simulation of progressive rock failure and associated seismicity. Int J Rock Mech Min Sci 34:249–261

Tang CA, Tham LG, Wang SH, Liu H, Li WH (2007) A numerical study of the influence of heterogeneity on the strength characterization of rock under uniaxial tension. Mech Mater 39:326–339

Van De Steen B, Vervoort A, Napier JAL (2005) Observed and simulated fracture pattern in diametrically loaded discs of rock material. Int J Fract 131:35–52

Wang SY, Lam KC, Au SK, Tang CA, Zhu WC, Yang TH (2006) Analytical and numerical study on the pillar rockbursts mechanism. Rock Mech Rock Eng 39(5):445–467

Wang SY, Sloan SW, Liu HY, Tang CA (2011) Numerical simulation of the rock fragmentation process induced by two drill bits subjected to static and dynamic loading. Rock Mech Rock Eng 44(3):317–332

Wang SY, Sloan SW, Sheng DC, Tang CA (2012a) Numerical analysis of the failure process around a circular opening in rock. Comput Geotech 39:8–16

Wang SY, Sloan SW, Tang CA, Zhu WC (2012b) A numerical investigation of the failure mechanism around tunnels in transversely isotropic rock masses. Tunn Undergr Space Technol 32:231–244

Weibull W (1951) A statistical distribution function of wide applicability. J Appl Mech 18:293–297

Wijk G (1978) Some new theoretical aspects of indirect measurements of the tensile strength of rocks. Int J Rock Mech Min Sci Geomech Abstr 15(4):149–160

Yu Y, Yin JM, Zong ZW (2006) Shape effects in the Brazilian tensile strength test and a 3D FEM correction. Int J Rock Mech Min Sci Geomech Abstr 43:623–627

Yu Y, Zhang JX, Zhang JC (2009) A modified Brazilian disk tension test. Int J Rock Mech Min Sci Geomech Abstr 46:421–425

Zhu WC, Tang CA (2006) Numerical simulation of Brazilian disc rock failure under static and dynamic loading. Int J Rock Mech Min Sci 43:236–252